Theses and dissertations

1-1-2011

Synthetic aperture imaging in acoustic microscopy

Golafsoun Ameri
Ryerson University

Synthetic Aperture Imaging in Acoustic Microscopy

by

Golafsoun Ameri

Bachelor of Engineering, Ryerson, 2009

A thesis

presented to Ryerson University

in partial fulfillment of the

requirements for the degree of

Master of Science

in the Program of

Biomedical Physics

Toronto, Ontario, Canada, 2011

©Golafsoun Ameri 2011

I hereby declare that I am the sole author of this thesis.

I authorize Ryerson University to lend this thesis to other institutions or individuals for the purpose of scholarly research.

_____

I further authorize Ryerson University to reproduce this thesis by photocopying or by other means, in total or in part, at the request of other institutions or individuals for the purpose of scholarly research.

_____

Synthetic Aperture Imaging in Acoustic Microscopy

Master of Science 2011

Golafsoun Ameri

Biomedical Physics

Ryerson University

Abstract

Acoustic microscopy (AM) provides micro-meter resolution using a highly focused single-element transducer. A drawback in AM is a relatively small depth of field, resulting in poor resolution outside the focus. Synthetic aperture focusing technique (SAFT) can be used to improve the image resolution throughout the field of view. SAFT mathematically synthesizes the effect of an array transducer and produces dynamic focusing and depth-independent resolution. SAFT in time domain with and without apodization, TD-SAFT and ATD-SAFT, respectively, and in frequency domain (FD-SAFT) were implemented and tested using simulated and experimental radio-frequency data from an acoustic microscope at 400 MHz. Lateral resolution of all the SAFT reconstructed images were better than those of the conventional B-mode images. While TD-SAFT and FD-SAFT performed better than ATD-SAFT in improving the lateral resolution, ATD-SAFT provided lower side lobes. In conclusion, SAFT improves resolution in AM outside the focal region.

Acknowledgements

Dedication

To my family

&

to my late childhood friend, Shiva, whose battle with leukemia did not allow her to

fulfill her lifetime dream of continuing her education

Contents

List of Tables

List of Figures

List of Appendices

Chapter 1

Introduction

1.1 Acoustic Microscopy and Its Applications

Imaging on the cellular level plays an increasingly important role in the evaluation of therapeutic response especially in cancer treatment [1]. Moreover, being able to observe processes as they happen within the cell adds a vital extra dimension to understanding cell functions [2]. A number of imaging-based methods have been developed that can detect cell death in tumor responses to treatment including single photon emission computed tomography, SPECT, and positron emission tomography, PET, [1]. However, SPECT and PET are expensive and require multiple injections of radiopharmaceuticals reducing their appeal for longitudinal studies of treatment effectiveness [1]. Therefore, since cost effective and non-invasive techniques would potentially have a high impact, studies have focused on employing ultrasound imaging for cell death monitoring and developing this imaging modality for the evaluation of treatment effectiveness [1], [3].

Ultrasound is the basis of 25% of all imaging procedures worldwide mostly due to its accessibility (i.e. portability and low cost), real time display, and non-ionizing radiation [4]. Moreover, cell imaging using ultrasound does not require contrast agents or molecular markers as the contrast is generated by the very process of cell death itself [3].

1

High frequency transducers need to be used in order to resolve scatterers at the cellular level in ultrasound imaging. Ultrasound imaging systems operating at frequencies above 100 MHz are referred to as acoustic microscopes which have applications in single cell studies. Acoustic microscopy was developed in the early 1970's by Lemons and Quate with applications in examining biological material using frequencies above 100 MHz [5]. Due to the large attenuation at such high frequencies, acoustic microscopy is not suitable for bulk tissue investigations. However, acoustic microscopy has the resolution and capabilities to resolve individual cells and organelles as they undergo biological processes [6]. Within the focal region of an acoustic microscope, high spatial resolutions approaching those of optical microscopy can be achieved. Additionally, acoustic microscopy has the advantage of not requiring cell staining, which is typically needed in optical microscopy [4], [7].

1.2 Image Quality and Beamforming

Acoustic beamforming modifies the propagation of sound waves through steering and/or focusing the beam. Beamforming plays an important role in the ultrasound image quality by affecting beam parameters such as the beam width, depth of field, and side lobe levels [8]. The depth of field is defined as the region of best lateral resolution along the ultrasound beam [9]. An overview on beamforming in single element transducers and array transducers is provided below.

Beamforming in single element transducers

In this case, the ultrasound beam is focused using a lens or a curved piezoelectric crystal resulting in a fixed focal length. By mechanically scanning the single element transducer over the region of interest (ROI), the focus of the transducer is steered. The motion of the transducer is electronically controlled by using a stepping motor-controlled positioning stage or a DC servo with custom actuators [10].

Beamforming in array transducers

Array transducers provide flexibility in beamforming in transmit and receive that is not possible with single element transducers. By controlling the time delay and weighting of each element of an array, beams can be focused, steered or shifted electronically at different depths. Adjustments of the length and apodization of the active aperture make changes in the lateral resolution and beam-shaping possible. Array beamforming creates dynamic focusing throughout the scan depth extending the depth of field to the whole region of interest [11].

In acoustic microscopy, a single element transducer is used since the fabrication of array transducers for use at high frequencies (above 30 MHz) is expensive and hard to achieve [12]. The highest center frequency of an array reported in the literature is at 80 MHz [12]. There are three main challenges in fabricating high frequency array transducers. First, an array design requirement is that the distance between the centers of two adjacent elements (i.e. an element pitch) should be less than one ultrasound wavelength in order to fully suppress grating lobes [13]. The element pitch at high frequencies would be very small, making the fabrication of such high frequency transducers with the available technology a challenging task [13]. For example, at 1 GHz, an element pitch of less than 1.5 μm is required [13]. Second, the high electrical impedance at high frequencies reduces the sensitivity of array transducers [13]. Finally, due to high cost and complexity, the beamforming electronics for applications at high frequencies are not commercially available yet.

As a result, single element transducers are used in acoustic microscopy. The fundamental problem concerning the design of a suitable ultrasound imaging system using a single element transducer is to find a compromise between a good axial and lateral resolution and the required penetration depth, which takes the attenuation into account [14]. In this regard, it is desired to employ a strongly focused transducer for two reasons. First,

high energy density in the short and narrow focal region could be obtained compensating the high attenuation of the signal energy by increasing the gain of the ultrasound transducer. Second, a narrow focal zone and a small F-number yielding a good lateral resolution could be obtained [14]. However, the drawback in employing a strongly focused transducer is that the depth of field becomes short limiting the region where conventional B-mode imaging has high resolution [14].

1.3   Synthetic Aperture Imaging

The concept of synthetic aperture imaging was first introduced in radar to detect, locate and provide high resolution images of remote targets on a terrain, a planet and so forth [15]. Synthetic aperture imaging is a pulse-echo technique in which the effect of a larger aperture is mathematically synthesized resulting in high resolution imaging. Synthetic aperture imaging techniques make depth independent resolution and dynamic focusing possible.

Similarly, ultrasound imaging is a pulse-echo method, in which ultrasonic waves illuminate a region of interest and the backscattered signals are used to form an image of the ROI which is based on its acoustic properties. Therefore, ultrasonic applications of the synthetic aperture technique follow directly from radar [16].

A short review of synthetic aperture (SA) imaging in radar and ultrasound is provided in sections 1.3.1 and 1.3.2.

1.3.1   Synthetic Aperture Radar

Synthetic aperture radar (SAR) is an airborne or satellite-borne radar system, which is considered as one of the most advanced engineering inventions of the twentieth century [15]. SAR offers improved image resolution by utilizing the movement of the radar antenna with respect to the target to synthesize the effect of a larger aperture. In SAR

imaging, a plane or satellite flies along a straight track. The antenna mounted on the aircraft emits pulses of electromagnetic radiation to illuminate the region to be imaged. These waves scatter off the terrain and are detected by the same antenna. The received signals are then used to produce an image of the terrain [17]. In synthetic aperture imaging, the scanning path is called the synthetic aperture or cross-range domain, which is denoted by y or u. The axial plane perpendicular to the scanning plane is called the range domain or the fast time domain as the propagation speed of the electromagnetic wave is much greater than the radar carrying aircraft and is denoted by x. The main SAR imaging algorithms are summarized as follows [15].

Stripmap SAR: This technique, which is also known as side-looking, is another SAR imaging modality introduced in 1950's. In this technique, a region much larger than the ROI is illuminated, so that the main lobe of the radar radiation pattern is not focused on a specific target region. Beam steering and focusing is applied as a post-processing technique on the acquired data to form an image of a specific part of the illuminated region.

Spotlight SAR: A more modern SAR imaging algorithm is spotlight SAR, which was developed in 1980's. This imaging modality utilizes mechanical or electronic beam steering of a physical radar in such a way that the region of interest remains illuminated completely while the platform goes across the synthetic aperture.

1.3.2 Synthetic Aperture Ultrasound

Synthetic aperture imaging based on stripmap SAR has been investigated in ultrasound imaging since the late 1960's and early 1970's [18]. In the 1970's and 1980's, it was primarily explored for non-destructive testing (NDT). With the advent of array transducers in the early 1980's, synthetic aperture was applied to array transducers for a

better signal-to-noise ratio and for fast data acquisition as mechanical scanning was not required any more. Until the beginning of 1990's, SA was rarely considered for medical ultrasound imaging applications. In 1992, a method for imaging the intravascular system utilizing the synthetic aperture imaging was developed [18]. The synthetic aperture algorithm used in ultrasound is referred to as the synthetic aperture focusing technique (SAFT) [19], which can be implemented in both time and frequency domain. The first implementation of SAFT was in the time domain and it was not until early 1980's that the frequency domain SAFT was developed [20].

The time domain SAFT is a delay-and-sum technique and the SAFT image is calculated by delaying the recorded echoes according to the imaging geometry, followed by coherent summation.

The frequency domain SAFT (FD-SAFT), which was introduced by Ermert and Karg [21], takes the form of a 2D spatio-temporal matched filter. Stepinski introduced a modified implementation of the FD-SAFT [22], which incorporates the diffraction effects of a finite size transducer.

The assumption in the SAFT is that that the transducer is a point source and the diffraction effects of the physical finite size radiation source are neglected. However, since the point source assumption is not a good approximation of ultrasonic transducers, the concept of a virtual source was introduced by Passman and Ermert in the early 1990's [23]. In the virtual source method, the focal point of the transducer is treated as a virtual point source producing spherical waves in the regions before and after the focus that radiate over a given angle, θ. Therefore, the diffraction effects of a large transducer are neglected for the virtual point source. Frazier and O'Brien studied the performance of a virtual source in terms of its effects on the lateral resolution, side lobe levels, spatial sampling rate, and SNR of SAFT reconstructed images at low frequencies [24].

Applications of SAFT in ultrasound imaging have been investigated by Karaman et al. [25] for small scale systems, Lockwood et al. [26] for sparse synthetic aperture

systems with the focus on 3D imaging applications, and by Nikolov et al. [27] for recursive ultrasound imaging.

SAFT has shown improved image resolution in comparison to the conventional B-mode imaging by making dynamic focusing and depth independent resolution using a single element transducer possible. SAFT been applications in non destructive testing using ultrasound for detection and characterization of defects in thick metal structures, especially in nuclear power plants [22].

1.4   Motivation and Hypothesis

The success of SAFT in low frequency ultrasound imaging inspired the study of SAFT in acoustic microscopy. As mentioned earlier, single element transducers are used in acoustic microscopy. Synthetic aperture imaging techniques make dynamic focusing and depth independent resolution possible.

The hypothesis of this thesis is that the SAFT in time domain and frequency domain will improve the lateral resolution of acoustic microscopy in the regions outside of the geometrical focus of the transducer in comparison to that of the conventional B-mode imaging technique.

1.5   Objectives

The specific objectives of this research project in testing this hypothesis are to:

- Simulate the transducer of an acoustic microscope operating at 400 MHz and obtain the radio-frequency data from point scatterers placed at different depths with respect to the focus of the transducer.

- Implement the time domain and frequency domain SAFT algorithms.

- Reconstruct images of the scatterers using the SAFT algorithms.

- Perform a quantitative analysis and comparison of the reconstructed images and conventional B-mode, CB-mode, images.

- Obtain experimental data and reconstruct images of the scatterers based on SAFT.

- Analyze the practical performance of the SAFT.

1.6   Outline of the Thesis

In Chapter 2, provides a short review on the acoustic field calculation as well as the theory related to the methods used in this thesis. Chapter 3 describes the methods used in the simulations and experiments to test the hypothesis. Chapter 4 provides the results obtained from simulations and experiments. Chapter 5 contains a discussion of the results by comparing the performance of the SAFT algorithms against the conventional B-mode imaging. The conclusion, significance and future work are provided in Chapter 6.

Chapter 2

Theory

2.1 Acoustic Field Calculations

The convolution representation of the radiated field developed by Tupholme and Stepan-ishen gives an exact solution to the wave equation for a transducer modeled as a planar rigid piston vibrating uniformly for any excitation waveforms [28, 29, 30, 31]. Based on this approach and the assumption of a uniform excitation across the transducer and a point scatterer, the received signal can be represented as,

$$p_r(\mathbf{r}, t) = \nu(t) \underset{t}{*} h_{pe}(\mathbf{r}, t), \tag{2.1}$$

where $p_r(\mathbf{r}, t)$ is the received pressure, $\nu(t)$ represents the excitation pulse convolved with the elecrto-mechanical impulse response during transmission and reception of the pulse, $h_{pe}(\mathbf{r}, t)$ is the pulse-echo spatio-temporal impulse response of the transducer, and $\underset{t}{*}$ is the convolution operator in the time domain. By assuming the transducer has the same spatio-temporal impulse response at transmit and receive, denoted by $h(\mathbf{r}, t)$, $h_{pe}(\mathbf{r}, t)$ can be calculated by,

$$h_{pe}(\mathbf{r}, t) = h(\mathbf{r}, t) \underset{t}{*} h(\mathbf{r}, t). \tag{2.2}$$

9

In order to calculate $p_r(\mathbf{r}, t)$ for different transducer geometries, the surface of the transducer can be divided into smaller mathematical elements, such as rectangles, to describe advanced shapes. Next, $p_r(\mathbf{r}, t)$ can be calculated for each small element [32]. For high precision calculations the size of the rectangles are chosen so that the field point lies in the far-field region [28]. As a result, a criterion to be satisfied is [28],

$$w \ll \sqrt{4lc/f_c},$$ (2.3)

where w is the largest dimension of the rectangle, l is the distance to the field point, f_c is the center frequency, c is the speed of sound, and λ is the wavelength. Finally, the responses from these elements are added together to give the field pressure at any point in the field.

An ideal plane wave is subject to attenuation during its passage through a medium [9]. Generally, attenuation depends on the frequency of the wave and is expressed as [9],

$$\alpha(f) = \alpha_o f^n,$$ (2.4)

where $\alpha(f)$ is the frequency dependent attenuation, α_o is a scaling factor with units that can be expressed in Np/(cm·MHz^n) or dB/(cm·MHz^n), f is the frequency of the wave, and n, which takes different values for different propagation mediums, lies in the range from 1 to 2 [9].

One approach to estimate the attenuated field is to use the attenuated impulse response $h_{att}(\mathbf{r}, t)$ instead of $h(\mathbf{r}, t)$ in equation(2.2), where $h_{att}(\mathbf{r}, t)$ is calculated by,

$$h_{att}(\mathbf{r}, t) = F^{-1}\{\alpha(f)\} \underset{t}{*} h(\mathbf{r}, t),$$ (2.5)

where $F^{-1}\{\cdot\}$ represents the Fourier inverse operator.

2.2 Conventional Ultrasonic B-mode Imaging

Displaying the echo information of a sequence of scan lines with brightness that is related to the amplitude of the signal is referred to as a *conventional* B-mode image in this thesis. The conventional B-mode image displays a slice of the region of interest in the axial plane. There are different methods of scanning the ROI based on the application; the scanning path could be along a straight line, i.e. a linear scanning, or along a curved path, also known as a sector scanning. Linear scanning is adapted in acoustic microscopy. The main limitation of conventional B-mode imaging using a single element transducer lies in the depth dependent lateral resolution in the image and SNR loss for weak scatterers [24]. The best resolution is achieved only for the part of the image containing echoes from the focus of the transducer [24]. Figure 2.1 shows a simplified block diagram of a conventional B-mode imaging system.

Details of the conventional B-mode imaging system are discussed below.

2.2.1 Time Gain Compensation

In order to compensate for the effects of attenuation, a method called time gain compensation is built into most medical ultrasound imaging systems to provide variable gain at different depths. The effect of these gains is that they provide a means to offset the loss in the signal caused by the variations in absorption and diffraction in the medium. Adjustments in time gain compensation are made to maintain an approximately uniform background level throughout the field of view. Note that the acoustic microscope used in this research study does not incorporate TGC in data acquisition.

2.2.2 Envelope Detection

In the conventional B-mode imaging, a method called envelope detection is used to detect the echoes from scatterers. The envelope of the echoed signal from a point scatterer is
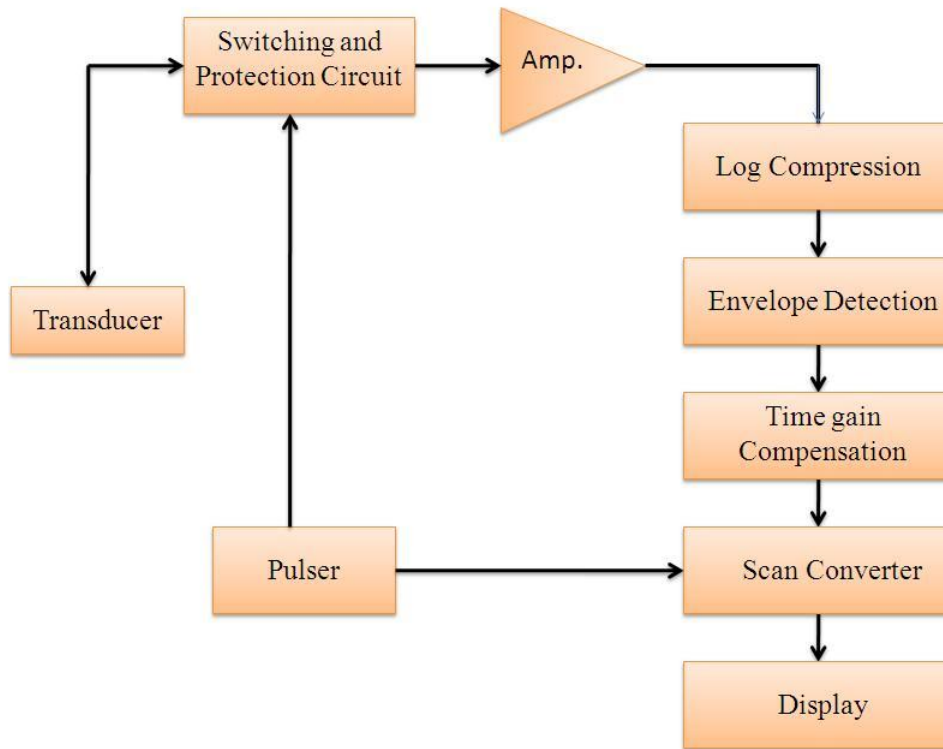
Figure 2.1: Block Diagram of a typical conventional B-mode imaging system. Adapted from [9].

the same as the envelope of the incident pulse if the frequency dependent effects in an ultrasound system are neglected [9]. An envelope detector then can provide an estimate of the envelope that closely matches the transmitted envelope. A straightforward method for determining the pressure envelope is through the Hilbert transform.

2.2.3   Logarithmic Compression

In ultrasound imaging, the signal dynamic range over which echoes can be reliably sensed may be as large as 150 dB. Therefore, signal compression is needed to avoid loss of information from such a large dynamic range when displayed on a device with a much

lower dynamic range (such as a video monitor). This is achieved by using logarithmic compression either through an analog logarithmic amplifier or by post processing the data. Logarithmic compression provides high gain for small signals and reduced gain for large signals thereby compressing the signal range [9]. A dynamic range of 40-60 dB is common in medical ultrasound systems [33].

2.2.4 Spatial Image Resolution

Spatial resolution of an imaging system is defined as the shortest distance between two point objects at which the objects can be dispalyed as distinct structures. Two objects are displayed as one if the resolution is insufficient. Spatial resolution in ultrasound imaging can be interpreted as the degree of smearing or blurring introduced to the image of a target.

Resolution is divided into two main categories: axial and lateral resolution. Axial resolution is the resolution in the direction of ultrasound propagation. Axial resolution depends on the length of the pulse used; a shorter pulse gives a higher axial resolution, but when the pulse becomes shorter, the sensitivity and penetration are reduced [11]. The axial resolution also depends on the ultrasound frequency as higher frequencies correspond to shorter wavelengths. The axial resolution, R_{axial}, is calculated by [9],

$$R_{axial} \approx \frac{c}{2\Delta f_{BW}}, \tag{2.6}$$

where c and Δf_{BW} denote the speed of sound and the bandwidth, respectively [9].

Lateral resolution is the resolution in the direction of scanning of the transducer. The lateral resolution of an electronic transducer depends on the width of the ultrasonic beam. The lateral resolution, $R_{lateral}$ is calculated by [9],

$$R_{lateral} \approx 1.22 F_{\#}\lambda, \tag{2.7}$$

where $F_{\#}$ denotes the F number [1] and λ is the wavelength. The above equations provide the dependency of lateral and axial resolution on some of the imaging system parameters. However, the resolution of an ultrasound image also depends on other parameters such as the pixel size and the signal to noise ratio (SNR) [2].

Moreover, if the point spread function (PSF) of an imaging system, which is defined as the response of the imaging system to a point scatterer is known, the resolution of the imaging system can be quantified using a measure called the full with at the half maximum (FWHM) [9]. This is the full width of the PSF at one-half of its maximum value. Therefore, if the PSF based on the backscattered pressure values are normalized to the maximum pressure value and expressed in dB, then the FWHM is equal to the lateral distance between the two points on the curve having the value of -6 dB. Percent reduction in FWHM (r_{FWHM}) of a SAFT reconstructed image from the FWHM of the conventional B-mode image at the location of a scatterer is obtained by,

$$r_{\text{FWHM}} = \frac{\text{FWHM}_{CB} - \text{FWHM}_{SAFT}}{\text{FWHM}_{CB}} \times 100\%, \tag{2.8}$$

where FWHM_{CB} represents the FWHM of the conventional B-mode image and FWHM_{SAFT} represents the FWHM of the SAFT image.

2.3 Apodization

Apodization refers to the amplitude weighting of the normal surface particle velocity across the aperture [11]. In array transducers, apodization on transmission is achieved by simply exciting individual elements in the array with different voltage amplitudes.

The primary effect of apodization is to increase the depth of field and to reduce the side lobes relative to the main lobe in the lateral direction [9]. The main lobe is referred

---

[1] $F_{\#}$ is defined as the focal length divided by the diameter of a concave transducer.
[2] SNR is defined as the ratio of the signal power to the noise power.
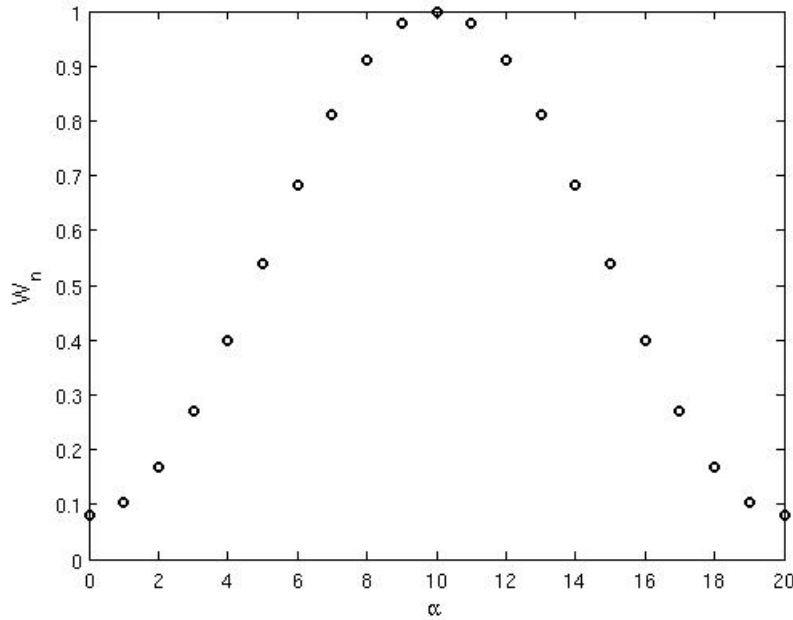
Figure 2.2: A Hamming window with $N = 21$.

to the lobe containing the maximum power and the side lobes, which have typically less signal power in comparison to the main lobe, are the lobes that exist on either side of the main lobe of a lateral profile[3]. It is desired to reduce the side lobes as they can appear to be echoes from scatterers [11]. Also, in conventional B-mode imaging strong reflectors in a beam profile's side lobe region can interfere with the interpretation of on axis targets [11]. However, the trade-off of apodization is the increase of the main lobe width, which results in degradation of the lateral resolution [9].

Therefore, it is important to choose an amplitude weighting function that would reduce the side lobes, but not result in a significant loss of resolution in the image. Raised cosine windows such as the Hamming window perform close to optimal in regards

---

[3]At a steady state, the field values along a lateral line drawn perpendicular to the axial direction of the wave propagation is called a lateral profile.

to leaving the image resolution intact [9]. The Hamming window is expressed as [34],

$$W_N(\alpha) = 0.54 - 0.46\cos(2\pi\frac{\alpha}{N-1}),$$ (2.9)

where N is the window size and $\alpha \in [0, N-1]$. Figure 2.2 shows an example of Hamming window with $N = 21$.

2.4 Wiener Filtering

Wiener filtering is the process of extracting the information-carrying signal $S(t)$ from the observed signal $Y(t)$, where $Y(t) = S(t) + N(t)$ and $N(t)$ denotes a noise process [35]. Wiener filtering can be used to reduce image distortion due to noise in ultrasound imaging [36, 37, 38, 39]. The goal in Wiener filtering is to extract the desired signal from the received signal based on the linear minimum mean-square error criterion [35]. Estimation of $S(t)$ from $Y(t)$ by the Wiener filter is done by minimizing the mean-square error estimate of $S(t)$. That is done by obtaining the optimum linear time-invariant filter such that the mean-square error estimate of $S(t)$ is minimum. Figure 2.3 illustrates a block diagram of such a system. The estimation of $S(t)$, which is the output of the filter is
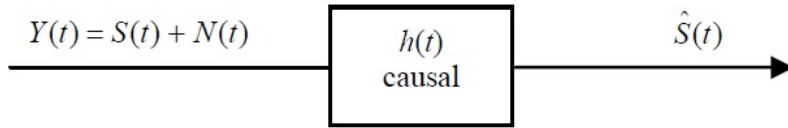
Figure 2.3: Optimum realizable Wiener filter

denoted by $\hat{S}$. Therefore, the error, $\varepsilon(t)$, and the mean-square error $E[|\varepsilon(t)|^2]$ are defined as,

$$\varepsilon(t) = S(t) - \hat{S},$$ (2.10)

and

$$E[|\varepsilon(t)|^2] = E[|S(t) - \hat{S}|^2]. \tag{2.11}$$

The Wiener filter minimizes $E[|\varepsilon(t)|^2]$. More details on a realizable Wiener filter, i.e. $h(t) = 0$ for $t < 0$, is provided in appendix A. In this work, Wienre filtering was done by using the *wiener2* function in MATLAB.

2.5 Synthetic Aperture Focusing Technique

As mentioned in section 1.3.2, the synthetic aperture focusing technique, is the synthetic aperture algorithm that is used in ultrasound imaging. This method has both time domain and frequency domain implementations both of which were implemented for this thesis. SAFT extends the limited depth of focus of a strongly focused transducer [40].

The following assumptions were used in the SAFT algorithms:

- point source: the radiation source is assumed to behave like a point source producing spherical waves. Therefore, the diffraction effects of the transducer are neglected in the image reconstruction.

- A constant speed of sound: it is assumed that the medium of propagation is homogeneous, non-dispersive, and non-attenuating. As a result the speed of sound is kept constant throughout the calculations in SAFT.

- isotropic scattering: it is assumed that the scatterers in the ROI scatter the wave isotropically and the reflectivity coefficient of scatterers is assumed to be frequency independent.

As mentioned in section 1.3.2, the focal spot of a focusing transducer can be treated as a point source. The small size of the focal spot makes a good approximation of a point source as it could represent a small source producing spherical waves. As shown
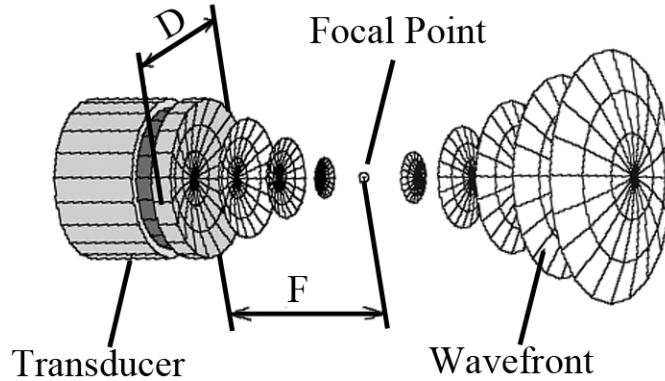
Figure 2.4: Idealized wavefront of a concave transducer. Reprinted from [10].

in figure 2.4, the wavefront of a concave transducer is a converging wave before the focal point and a diverging spherical wave after the focus, similar to a point source. The virtual source can be scanned by scanning the physical transducer. The feasibility of treating the geometrical focal spot of a transducer as a virtual source was studied in [24] and [41]. It was also concluded in [24] that better lateral resolution can be achieved for a tightly focused transducer in comparison to moderately focused transducers when using virtual point SAFT reconstructions.

Before the SAFT reconstructions are done, a virtual point source is created. This can be done by truncating the RF data at the time sample corresponding to the focus. For reconstruction in regions before the focus, RF data could be reversed in time.

The SAFT algorithm relates the signal intensity at each image point to the sum of the appropriately delayed backscattered signals at different scan locations to form an image function of the region of the ROI [42].

The details of the SAFT algorithm in time and frequency domain are provided below.

2.5.1 Time Domain SAFT (TD-SAFT)

One of the main assumptions in SAFT is that the radiation from the (virtual) source is uniform over an aperture angle, θ. As a result, the diffraction effects of the transducer used for scanning can be neglected due to the point source assumption [43]. Therefore, if the displacement increments in the lateral direction of a transducer during linear scanning are small enough, the sound filed generated by the virtual source at a given scan position will overlap with the sound filed produced at the adjacent positions [40]. Figure 2.5 shows a schematic of data acquisition for a concave transducer, where the transducer's first scan location is denoted by u_{n_i} and its final location by u_{n_f}. The step size between two consecutive transducer locations is denoted by d_u. In this figure, the focus of the transducer, at location $x = x_f$, can be treated as a virtual source which is moved by d_u increments along the y-axis.
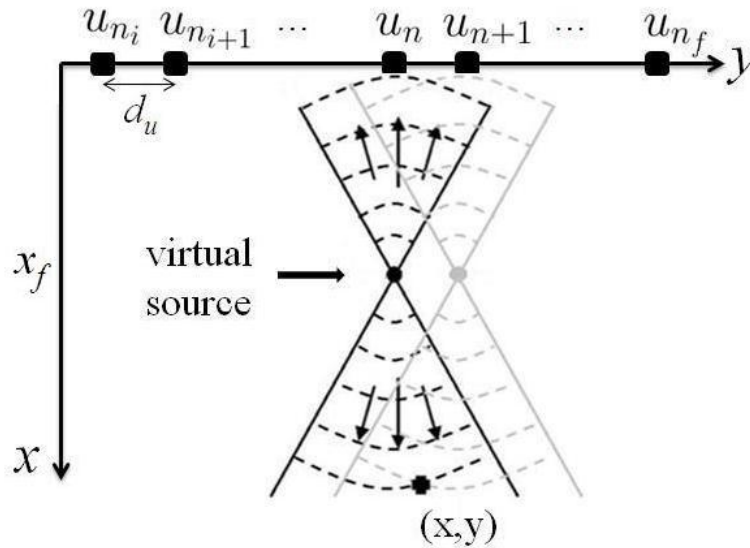
Figure 2.5: Schematic of the virtual source concept.

In this schematic the location (x, y) is in the overlapping region of the acoustic fields at transducer locations u_n and u_{n+1}. Therefore, at these transducer locations, the obtained

19

RF data samples which correspond to the backscattered echoes from the region after the virtual source can be used to synthetically focus at location (x, y).
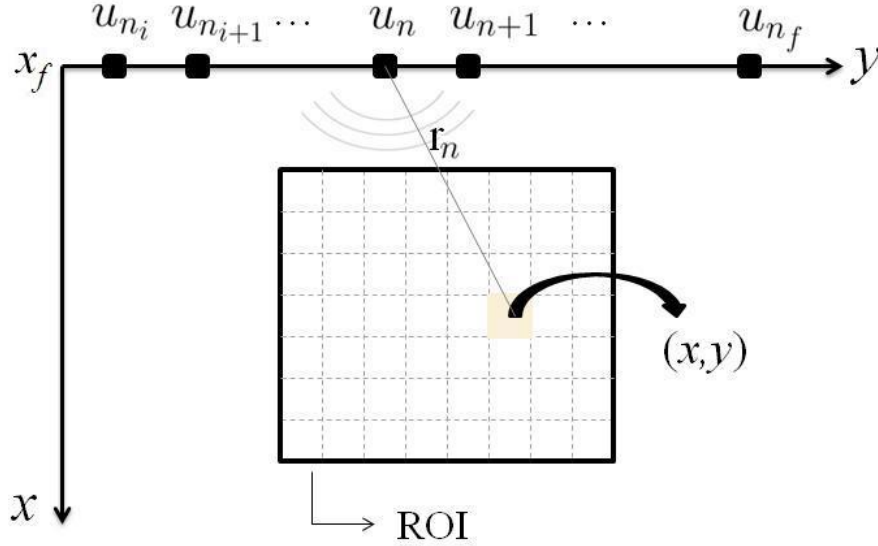
Figure 2.6:   Schematic of synthetic focusing in time domain SAFT.

In order to derive a mathematical expression of synthetic aperture focusing on any point in a ROI, figure 2.5 is simplified to show the region after the transducer's focal point as shown in figure 2.6. The y-axis is drawn at $x = x_f$. As shown in this figure, the locations of the virtual source, shown on the y-axis, are the same as the positions of the physical transducer along the y-axis. Therefore, the first virtual source location is denoted by u_{n_i} and its final location by u_{n_f}. The black rectangle represents the region of interest and the dashed lines delineate the pixels of the image from the ROI. In order to focus on any pixel location at (x, y), the distance r_n, from the virtual source locations to location (x, y) is calculated by,

$$r_n = \sqrt{x^2 + (y - u_n)^2},$$ (2.12)

where $u_n \in [u_{n_i}, u_{n_f}]$. If $s(t, u)$ is the acquired echo data at time t and at a scan location u, then the image function value at location (x, y) is calculated by,

$$f_{\text{TD}}(x, y) = \sum_{n=n_i}^{n_f} S\left(\frac{2r_n}{c}, u_n\right). \tag{2.13}$$

The RF samples from the region before the virtual source are used to synthetically focus on a point before the geometrical focus of the transducer.

Apodization is usually applied in the time domain SAFT to decrease the side lobe levels. A Hamming window is used for apodization with $N = n_f - n_i + 1$. Therefore, the apodized $f(x, y)$ denoted by $f_{\text{ATD}}(x, y)$ is obtained by,

$$f_{\text{ATD}}(x, y) = \sum_{n=n_i}^{n_f} W_N(n - n_i) S(\frac{2r_n}{c}, u_n), \tag{2.14}$$

where $W_N(n - n_i)$ is the window function as described in section 2.3. The TD-SAFT that includes apodization in image reconstruction is denoted by ATD-SAFT.

In TD-SAFT, the focus of a concave transducer is treated as a virtual source emitting spherical waves over a certain aperture angle 2θ, as shown in figure 2.7.
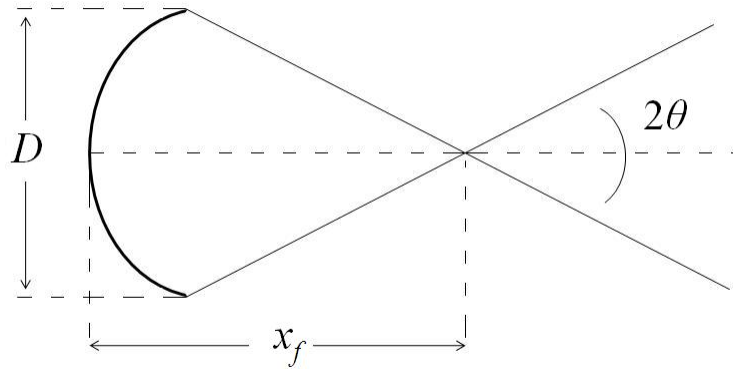
Figure 2.7: Schematic of a concave transducer beam.

The half aperture angle at which the beam spreads can be approximated by [24],

$$\theta = \tan^{-1}\left(\frac{D}{2x_f}\right),$$

(2.15)

where D is the diameter of the transducer. As illustrated in figure 2.8, based on the
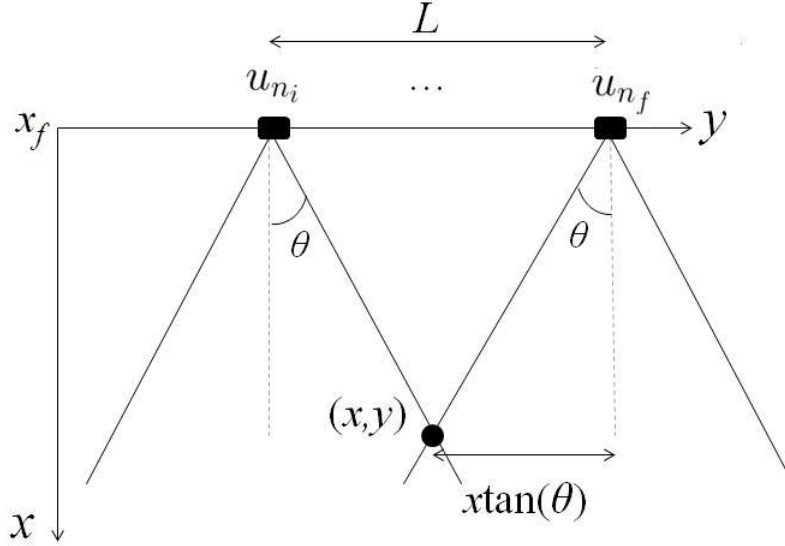
Figure 2.8: Determination of scan length and location.

aperture angle, the acoustic field from a limited number of transducer locations overlap at location (x, y). The transducers at locations before u_{n_i} and after u_{n_f} do not insonify the location (x, y). The limits of the aperture are given by,

$$u_{n_i} = y - \frac{L}{2} \quad \text{and} \quad u_{n_f} = y + \frac{L}{2}.$$

(2.16)

where $L = 2x\tan(\theta)$. As the location (x, y) gets farther from the virtual source, L increases. The scan location indices corresponding to the u_{n_i} and u_{n_f} locations are given by,

$$n_i = \frac{u_{n_i}}{d_u} \quad \text{and} \quad n_f = \frac{u_{n_f}}{d_u}.$$

(2.17)

22

2.5.2 Frequency Domain SAFT (FD-SAFT)

In the frequency domain SAFT (FD-SAFT) algorithm, it is assumed that a point source scans the ROI along an infinite scan length, L. Figure 2.9 shows the ideal SA imaging geometry where point sources are scanned over an infinite SA length, i.e. $u \in (-\infty, \infty)$. At each transducer location, the point source emits a short pressure pulse (i.e. broad band) $p(t)$. Therefore, a spherical wave propagates in the medium omni-directionally. For each point scatterer, the location and the reflectivity coefficient are given by (x_i, y_i) and σ_i, respectively.
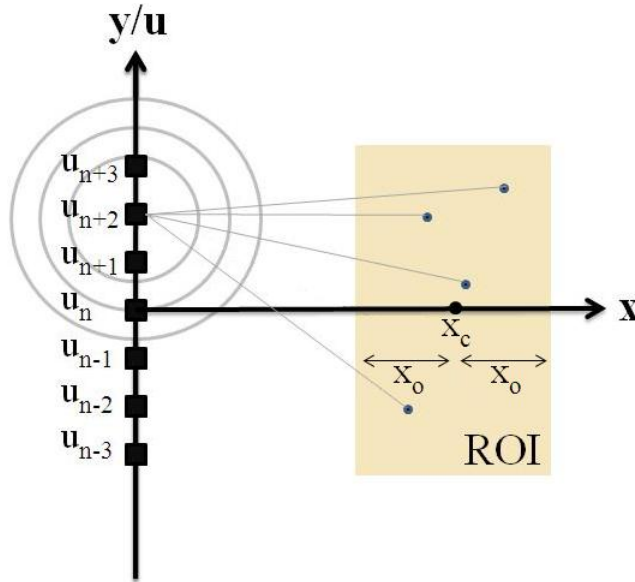
Figure 2.9: Schematic of the FD-SAFT imaging system. Adapted from [10].

The received pressure wave at each scan location is given by [15],

$$s(t, u_n) = \sum_i \sigma_i p[t - \frac{2\sqrt{x_i^2 + (y_i - u_n)^2}}{c}], \tag{2.18}$$

where $\frac{2\sqrt{x_i^2 + (y_i - u_n)^2}}{c}$ is the round trip time delay from the transducer at the location u_n

23

to the ith target. Note that the time axis is along the x-axis and u, the synthetic aperture axis, is along the scanning path, i.e. y-axis. The ideal target function, which would result in the image of the region of interest, in the spatial domain is given by [15]:

$$f_o(x, y) = \sum_i \sigma_i \delta(x - x_i, y - y_i). \tag{2.19}$$

The inverse problem in SA imaging is to obtain the target function, also known as the image function, based on the received echo signals. An approach to obtain the target function is to first take the 2D Fourier transform of the received RF lines. This is shown in two steps in the following equations, where equation (2.20) shows the Fourier transform of $s(t, u)$ with respect to time, resulting in $s(\omega, u)$, and equation (2.21) shows the Fourier transform of $s(\omega, u)$ with respect to u, resulting in $S(\omega, k_u)$, where k_u represents the spatial frequencies in the cross-range domain [15].

$$s(\omega, u) = P(\omega) \sum_i \sigma_i \exp[-j2k\sqrt{x_i^2 + (y_i - u)^2}], \tag{2.20}$$

$$S(\omega, k_u) = P(\omega) \sum_i \sigma_i \underbrace{\exp(-j\sqrt{4k^2 - k_u^2}x_i - jk_u y_i)}_{\text{a linear phase function of } (x_i, y_i).} \tag{2.21}$$

Next, the 2D spatial Fourier transform of $f_o(x, y)$ with respect to x and y is obtained [15].

$$F_o[k_x(\omega, k_u), k_y(\omega, k_u)] = \sum_i \sigma_i \exp(-jk_x x_i - jk_y y_i), \tag{2.22}$$

where

$$k_x(\omega, k_u) = \sqrt{4k^2 - k_u^2}, \tag{2.23}$$

$$k_y(\omega, k_u) = k_u, \tag{2.24}$$

and

$$k = \frac{\omega}{c}, \tag{2.25}$$

where k_x is the spatial frequency or wavenumber domain for range x, k_y is the spatial frequency for cross range y, and k is the wavenumber.

By comparing equations (2.21) and (2.22), the following expression is derived [15],

$$S(\omega, k_u) = P(\omega) F_o[k_x(\omega, k_u), k_y(\omega, k_u)]. \tag{2.26}$$

Therefore, the 2D Fourier transformed target function is given by,

$$F_o[k_x(\omega, k_u), k_y(\omega, k_u)] = \frac{S(\omega, k_u)}{P(\omega)}. \tag{2.27}$$

However, the above equation is a theoretical reconstruction of F_o and it is not realizable as $p(t)$ is a band-limited signal, i.e. it has a finite support in the ω domain. The practical reconstruction is via fast-time matched filtering as follows [15],

$$F[k_x(\omega, k_u), k_y(\omega, k_u)] = P^*(\omega) S(\omega, k_u), \tag{2.28}$$

for $k_u \in [-2k, 2k]$. Due to the nonlinear nature of the two-dimensional mapping from the (ω, k_u) domain into the (k_x, k_y) domain, the resultant image function $F(k_x, k_y)$ is unevenly spaced. However, the knowledge of $F(k_x, k_y)$ on a uniform rectangular grid is required in order to obtain the image function $f_{\text{FD}}(x, y)$ in the spatio-temporal domain via a two dimensional Fourier transform [15].

Figure 2.10 shows the unevenly sampled data as circles and the desired evenly spaced data as the filled black squares. The mapping from k_u to k_y is evenly spaced, since $k_y = k_u$. However, the mapping from ω to k_x is nonlinear as $k_x = \sqrt{4k^2 - k_u^2}$. This mapping is done via a windowed sinc interpolation as follows,
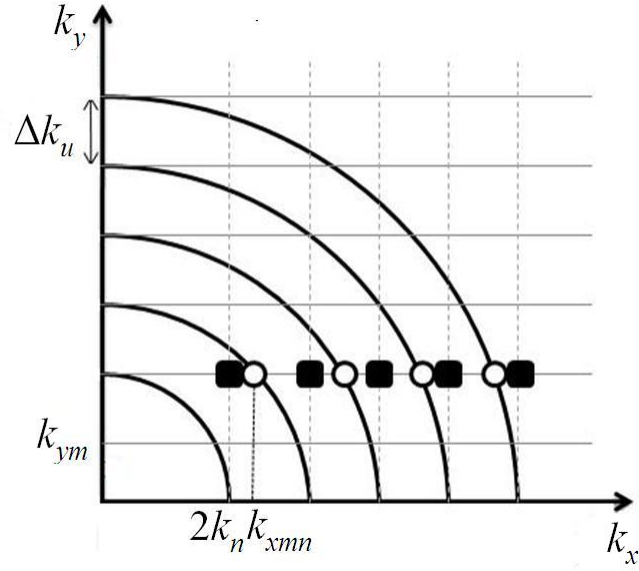
Figure 2.10: Spatial frequency mapping for discrete data. Adapted from [15].

$$F(k_x, k_{ymn}) \approx \sum_{|k_x - k_{xmn}| \leq N_s \Delta k_x} F(k_{xmn}, k_{ymn}) h_\omega(k_x - k_{xmn}), \tag{2.29}$$

where

$$h_\omega(k_x) = \begin{cases} h(k_x)\omega(k_x) & , |k_x| \leq N_s \Delta k_x \\ 0 & , \text{Otherwise} \end{cases}, \tag{2.30}$$

$$h(k_x) = sinc(\frac{k_x}{\Delta k_x}), \tag{2.31}$$

and

$$\omega(k_x) = \begin{cases} 0.54 + 0.46 \cos(\frac{\pi k_x}{N_s \Delta k_x}), & |k_x| \leq N_s \Delta k_x \\ 0, & \text{otherwise} \end{cases}. \tag{2.32}$$

The Nyquist sampling criterion in the synthetic aperture domain and the range do-

main are

$$\Delta k_u = \frac{2\pi}{M\Delta u}, \tag{2.33}$$

and

$$\Delta k_x \leq \frac{\pi}{X_o}, \tag{2.34}$$

where M is the number of scan locations and X_o is the half-size of the target area in the range domain.

Chapter 3

Methods

The SAFT algorithm was implemented in both time domain (TD-SAFT and ATD-SAFT) and frequency domain (FD-SAFT). In ATD-SAFT apodization in receive was performed by utilizing a Hamming window. The TD-SAFT implementation was verified against published results and the performance of the synthetic aperture focusing technique in acoustic microscopy was investigated in both simulation and experimental setups.

The simulation parameters were based on the acoustic microscope used to obtain experimental data which was available in the *Advanced Biomedical Ultrasound Imaging and Therapy Laboratory* at Ryerson University. The main features of the acoustic microscope used in this research are presented in section 3.1. Section 3.2 provides the details of simulations used in the TD-SAFT implementation verification. Section 3.3 dicusses the simulation of an acoustic microscope as well as the SAFT algorithms used for reconstruction images from the simulated data. The experimental setups and procedures are provided in section 3.4.

3.1   SASAM Acoustic Microscope

In this study, the SASAM® IN acoustic microscope (Kibero GmbH, St. Ingbert, Germany) was used to acquire experimental data. An image of the entire system is shown in figure 3.1. The SASAM microscope is specifically designed for the quantitative imaging of the mechanical properties and morphology of single cells, cell layers, and *ex vivo* biopsies [44].

Figure 3.1: The SASAM acoustic microscope retrieved from [44].

The acoustic microscope consists of an optical and an acoustic module.

Optical Module

The acoustic microscope is equipped with an IX81 optical microscope (Olympus Optical Co., Ltd., Tokyo, Japan). During acoustic measurements, the optical microscope can be used in the reflection mode to allow for visualization and precise alignment of the acoustic tip to specific regions of interest within the sample [45]. Moreover, the optical microscope is capable of taking high contrast optical images with phase contrast from the sample before or after the acoustic data acquisition.

Acoustic Module

The acoustic microscope is equipped with three different transducers with the center frequencies of 205 MHz, 375 MHz, and 1.2 GHz. The focusing cavity of these transducers are spherical in shape. Properties of the transducers are provided in table A, which was obtained from [6]. In this thesis, the transducer with the center frequency of 375 MHz was used.

Table 3.1: Transducers' properties measured at 36°C.

Center Frequency (MHz)	-6 dB Bandwidth	Focal Length (μm)	Aperture Width in (μm)	Aperture Angle (°)
205	49 %	500	500	60
375	42 %	335	350	60
1250	30 %	50	50	100

The backscattered echo from a planar glass reflector placed at the focus of the 375 MHz transducer is shown in figure 3.2. This signal is referred to as the reference signal and is used in the FD-SAFT.

3.1.1 Positioning the Transducer and Sample

There are two separate electronics modules used in the acoustic microscope to control the position of the transducer and the sample with respect to each other. The first module is

(a)   (b)
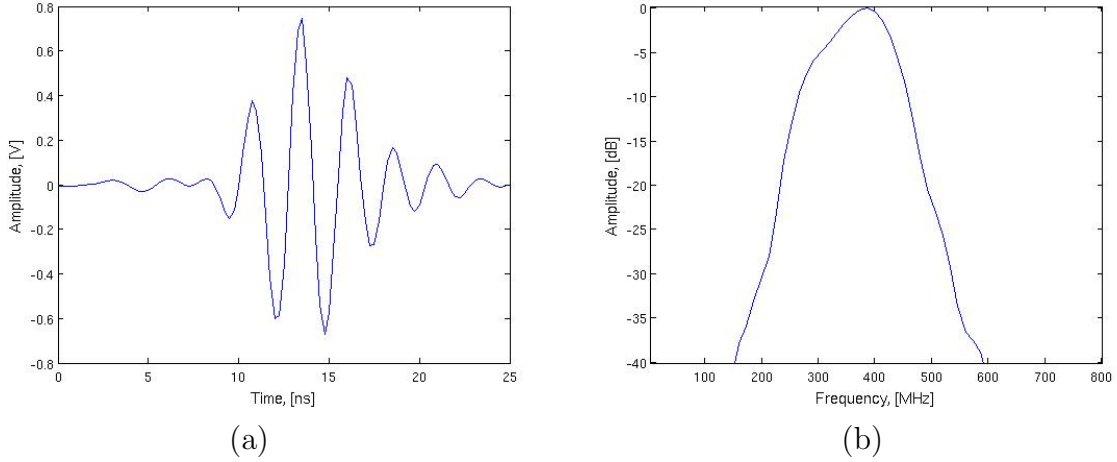
Figure 3.2: The 375 MHz SASAM transducer's pulse signal and its frequency spectrum.

the Corvus stage controller (ITK Dr. Kassen GmbH, Lahnau, Germany) which can move the sample under the microscope in the 2D lateral plane with respect to the transducer with a minimum step size of 1.5 nm allowing for precise alignment of the sample. This module is controlled by the operator with a joystick. The second module is a piezo controller ENT400 (Piezosystem Jena GmbH, Jena, Germany) which can control the movement of the transducer in the lateral and axial directions. The step size of this module ranges from 0.1 μm to 2.0 μm.

3.1.2 Noise and Artifacts

Similar to medical ultrasound imaging, one of the main sources of noise in acoustic microscopy is electronic noise. This type of noise is considered additive and can mostly be eliminated by filters. One major source of noise in acoustic microscopy, which cannot be removed by a filter, is due to the ultrasound propagation through the transducer rim. As shown in figure 3.3, the ultrasonic waves traveling through the rim and through the lens propagate in the medium and their reflections from the substrate are received by the transducer. The speed of sound in sapphire, which constructs the main body of the

31
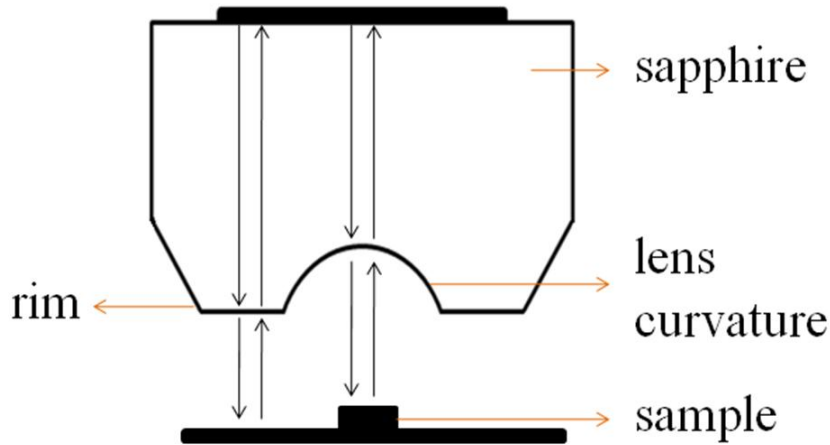
Figure 3.3: Ultrasound wave path in the transducer, adopted from [6].

transducer, is approximately 11,150 m/s, while the speed of sound in water, the medium of propagation, is around 1,500 m/s [46]. Although, the travel path for waves going through the sapphire or the curved lens is the same, due to the difference in the speed of sound of sapphire and water, the echoes from the substrate measured through the rim will appear ahead of the measured echoes through the curved lens. The desired echoes are those that go through the focused transducer lens. However, the echoes passing through the rim of the transducer are not desired and result in artifacts in the image. Therefore, during data acquisition, one should make sure that echo from the region of interest in the sample is sufficiently separated from the substrate echo as well as the rim echo.

3.2 Verification of TD-SAFT

A specialized TD-SAFT algorithm, where L was constant and independent of the pixel location, was used to verify the TD-SAFT implementations against published results in [22]. In this case, $L = 9.5$ mm.

In order to verify the TD-SAFT implementation, the TD-SAFT reconstructed image

of a point scatterer presented in [22] was reproduced. The impulse response of the piston transducer obtained from [22] was used to simulate backscattered RF data from the transducer using Field II.

Field II is a powerful software tool, which has been developed to calculate the pressure filed emitted from an arbitrary shape, apodized, and excited ultrasound transducer for linear propagation [28], and to calculate the received echo from simulated scatterers [47]. More than 60 journal articles have been published from its use by a large number of research groups [48]. This program is based on the Tupholme-Stepanishen method explained in [29] and [30] for calculating ultrasound fields as described in section 2.1.

The transducer was simulated in Field II and a scatterer was placed 40 mm away from the piston transducer in the simulation. The simulation parameters for the piston transducer are provided in table 3.2. All the values in this table were obtained from [22]. Finally, the image of the scatterer was reconstructed using the TD-SAFT and visually compared to the TD-SAFT image in [22]. The synthetic aperture used for the TD-SAFT consisted of 20 scan locations, with L equal to 9.5 mm. A lateral distance of 60 mm over the scatterer along the synthetic aperture axis was scanned. In the TD-SAFT implementation, it was assumed that the piston transducer behaved similar to a point source and as a result the diffraction effects of the physical aperture were neglected. In addition to the TD-SAFT, the FD-SAFT implementation was also used to reconstruct the image of the scatterer. The results are shown in section 4.1.1.

3.3   SAFT in Acoustic Microscopy

Simulations of the acoustic microscope were performed in order to quantitatively analyze the performance of SAFT in acoustic microscopy as it is easy to control and change simulation parameters in comparison to experiments.

The 375 MHz concave transducer of the SASAM acoustic microscope was modeled

Table 3.2: Simulation parameters for a piston transducer.

Parameter	Notation	value	Unit
Transducer diameter	D	4	mm
Center frequency	f_c	1.5	MHz
Sampling frequency	f_s	84.2	MHz
Speed of sound	c	1540	m/s
Scatterer position	Z_p	40	mm
Scan step size	d_u	0.5	mm

in Field II. The simulation parameters are provided in section 3.3.1. TD-SAFT, ATD-SAFT, and FD-SAFT were used to reconstruct images of point scatterers in the simulations. In all cases, the focus of the transducer was treated as a virtual point source.

The SAFT performance was quantitatively analyzed based on the FWHM and side lobe levels of the obtained images at the location of the scatterers. The FWHM of different SAFT algorithms were also compared to those values obtained from the conventional B-mode image of the simulated data.

Wiener filtering was applied before processing and its effect on the images was investigated.

3.3.1 Simulation of an Acoustic Microscope

The 375 MHz transducer of SASAM, which was a concave transducer with a tight focus, was simulated in Filed II. The simulation parameters are provided in table 3.3.

The impulse response (IR) of the concave transducer used for Filed II simulations is shown in figure 3.4. The IR used in the simulations was a Hamming windowed sinusoidal function with a center frequency of 375 MHz and sampling frequency of 4 GHz. This IR was chosen as it was similar to the reference signal of the transducer.

Table 3.3:   Simulation parameters for a concave transducer.

Parameter	Notation	value	Unit
Aperture diameter [44]	D	291	μm
Center frequency [44]	f_c	375	MHz
Sampling frequency	f_s	4	GHz
Speed of sound [9]	c	1540	m/s
Focal length [44]	x_f	335	μm
Scan step size	d_u	1	μm
Attenuation coefficient at f_c [9]	α	400	dB/cm
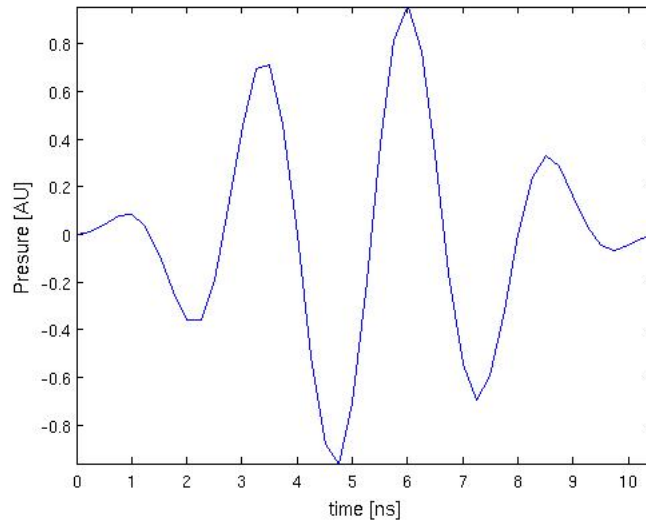
Figure 3.4:   The IR used in the concave transducer simulations.

Five point scatterers located at different depths along the same axial line were all located before the focus of the concave transducer in one simulation and after the focus in another simulation. As mentioned previously, the focal spot of the transducer is treated as a virtual source. Therefore, the RF data corresponding to the region after the focus or

before the focus are used in SAFT to reconstruct images of scatterers that are either after or before the virtual source, respectively. As a result, image reconstruction of scatterers at the focus is not possible with SAFT. Hence, no scatterer was placed at the focus of the transducer.

The y coordinate of all the scatterers was 0. The scanning was done from -600 μm to 600 μm along the y-axis. The reconstructed images show a region that start from -300 μm to 300 μm on the y-axis. Frequency independent attenuation in the medium was included in the simulations and white Gaussian noise was added to the simulated data in order to analyze the performance of SAFT for noisy data as well as to study the effect of the Wiener filter on ultrasound backscattered data. Noise was added to the RF data using the *awgn* function in MATLAB, which takes the RF data and the SNR of interest in dB in its argument. This function adds white Gaussian noise to the input matrix so that the output data has an SNR equal to the desired value. Two different RF data sets with the arbitrary chosen SNRs of 10 dB and 5 dB were obtained.

3.4 Experimental Evaluation Using an Acoustic Microscope

Experiments were performed in order to qualitatively analyze the performance of the different image reconstruction techniques. The experimental RF data of micro-beads were obtained with the SASAM system and the 375 MHz transducer. The experimental parameters were the same as those used in the simulations provided in table 3.3. The micro-beads were in a powder form consisting of carbon beads with diameters ranging from 2 μm - 12 μm. The phantom was prepared by mixing the agar powder with water and the carbon beads. The mixture of agar and water formed a gel that kept the micro-beads fixed in place. Agar mimics tissue acoustic properties, which makes it a suitable propagation medium in ultrasound imaging [49].

The phantom was placed on a glass substrate and drops of water were added on top of the sample. Water was used as the coupling fluid between the transducer and the agar gel. A micro-particle would be located using the optical images obtained from the optical module and a corresponding region of interest would be chosen. Then, the transducer would be moved to be placed over the ROI. The positioning of the transducer over the particle was done by aligning the cross present on the optical lens to the center of the transducer appearing in the optical image. Next, a 1-D scan was performed. In order to reduce noise in the RF data, a Butterworth bandpass filter with a frequency range of 100 to 800 MHz was utilized during data acquisition. Measurements were averaged 400 times to improve the SNR. In order to reduce other artifacts, the signal received from the medium without the presence of any scatterer was subtracted from the RF lines obtained from scanning the region of interest. The transducer was moved in the vertical direction in order to obtain RF data from the bead at different depths.

In addition to the RF data from micro-beads, RF data of a spheroid were obtained. The spheroid was produced from MCF-7 breast cancer cells (ATCC, Manassas, VA). Spheroids are spherical, heterogeneous aggregates of cells in culture medium. They represent an *in-vitro* model for studies of both normal and malignant cells. Prior to the experiment, the spheroid was transferred to a chamber slide (NUNC, Germany), which has a raised edge to hold biological specimens and liquids.

The spheroid started growing and expanding on the chamber slide. Therefore, the radius of the spheroid's surface on the glass, i.e. 80 μm, was slightly larger than its thickness of 60 μm as shown in figure 3.5.

The spheroid was kept in cell culture medium, which could be used as a coupling medium. The tip of the transducer was placed inside the chamber into the culture medium during data acquisition.

The focus of the transducer was placed once just above the spheroid at around 60 μm from the glass substrate, and once at 115 μm above the glass. In figure 3.5, the red circles
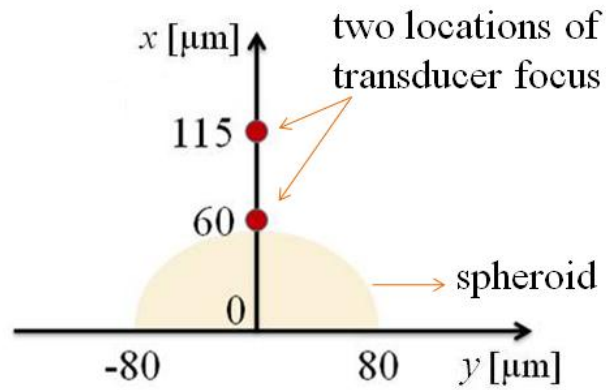
Figure 3.5: The schematic of the spheroid experiments.

indicate the distance between the focus of the transducer from the chamber slide during two different sets of data acquisitions.

Chapter 4

Results

4.1 Simulations

4.1.1 Verification: Piston Transducer

This section provides the reconstructed images based on the properties of the transducer used in [22]. Figure 4.1 (a) shows the image, $f'_{TD}(x, y)$, presented in [22] from a scatterer placed at 40 mm away from a piston transducer. Figure 4.1 (b) shows the reconstructed image, $f_{TD}(x, y)$ defined by equation 2.13, of the same target using TD-SAFT. The reconstructed image of the target using the FD-SAFT is provided in figure 4.2.
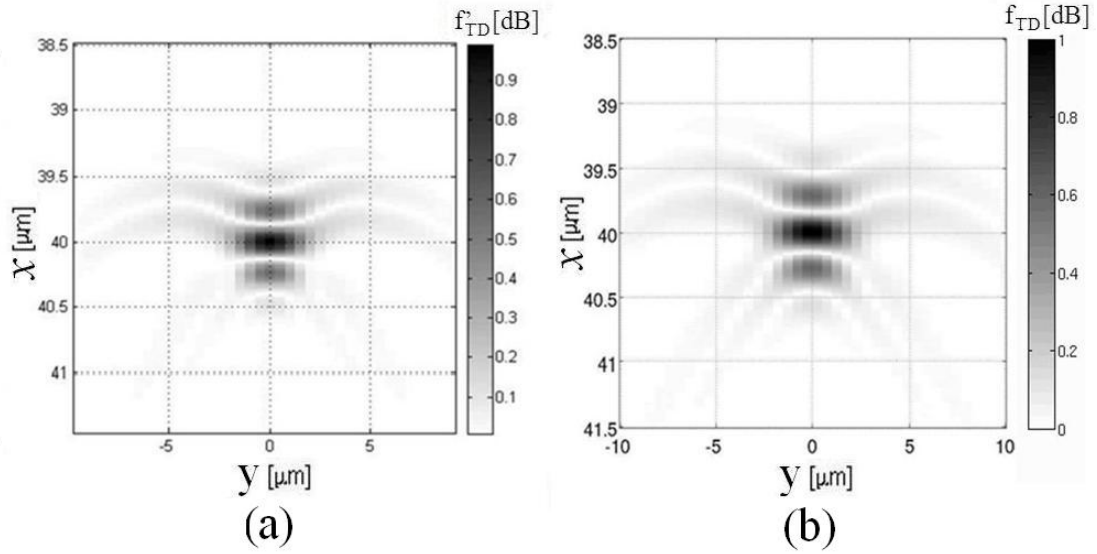
Figure 4.1: The TD-SAFT reconstructed image of a scatterer (a) presented in [22] and (b) reproduced for the TD-SAFT implementation verification.
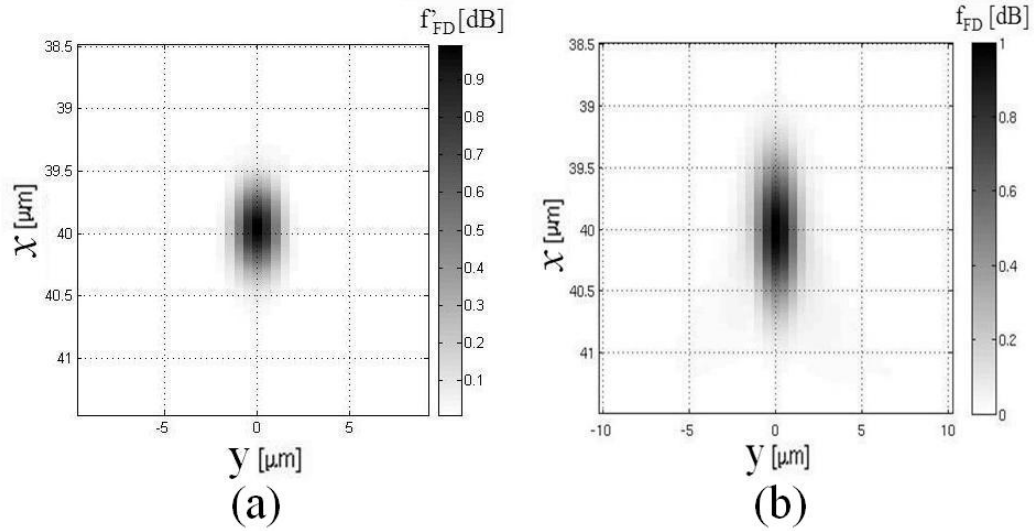

Figure 4.2: Reconstructed image of a scatterer using (a) modified FD-SAFT, which incorporates the diffraction effect of the piston transducer, presented in [22], and (b) FD-SAFT assuming a point transducer, with no diffraction effects.

4.1.2 Concave Transducer

Five point scatterers were placed either all before or all after the focus in the Field II simulation of the SASAM transducer. Images of the scatterers were obtained using the conventional B-mode imaging and synthetic aperture focusing techniques. Section 4.1.2.1 provides the results for the RF data set with an SNR of 10 dB and section 4.1.2.2 provides the images based on the RF data with a 5 dB SNR. Note that the focus of the transducer in the all of the images in this section is at 335 μm.

4.1.2.1 Image Reconstruction With 10 dB SNR

a) All Scatterers Before the Focus
Figure 4.3 (a) and (b) illustrate the conventional B-mode images without and with Wiener filtering, respectively, of the five scatterers. As shown in figure 4.3 (b), the Wiener filter was effective in reducing the additive white Gaussian noise level. Therefore, all the simulated and experimental data were Wiener filtered before processing.

The reconstructed images of the scatterers placed before the focus from 85 μm to 285 μm, with a step-size of 50 μm, using TD-SAFT, ATD-SAFT, FD-SAFT and conventional B-mode imaging method are shown in figure 4.4 (a)-(d), respectively.

The lateral profiles of the images with an SNR of 10 dB at the location of the scatterers placed before the focus are shown in figure 4.5.
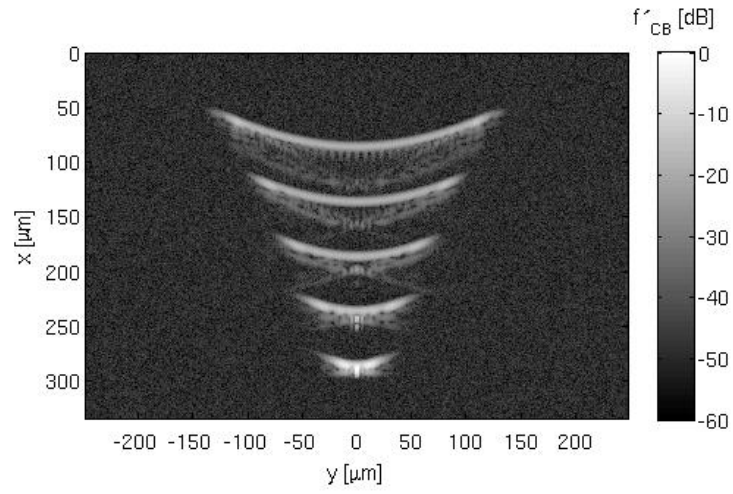
(a)
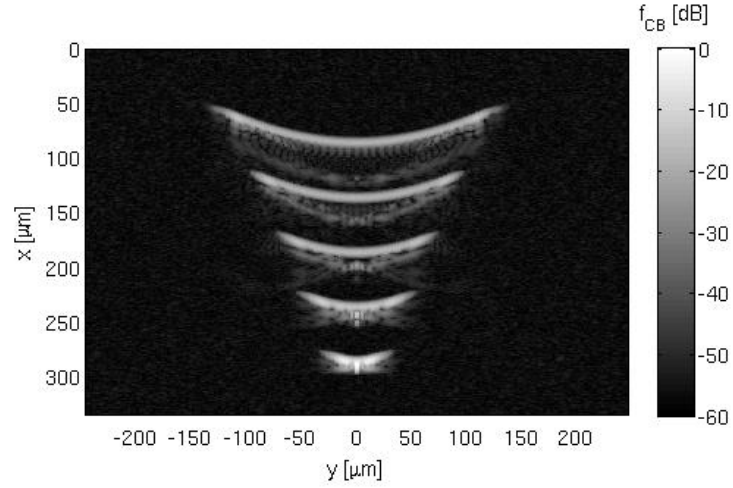
(b)

Figure 4.3: The conventional B-mode image of five point scatterers placed before the focus, (a) without and (b) with Wiener filtering.
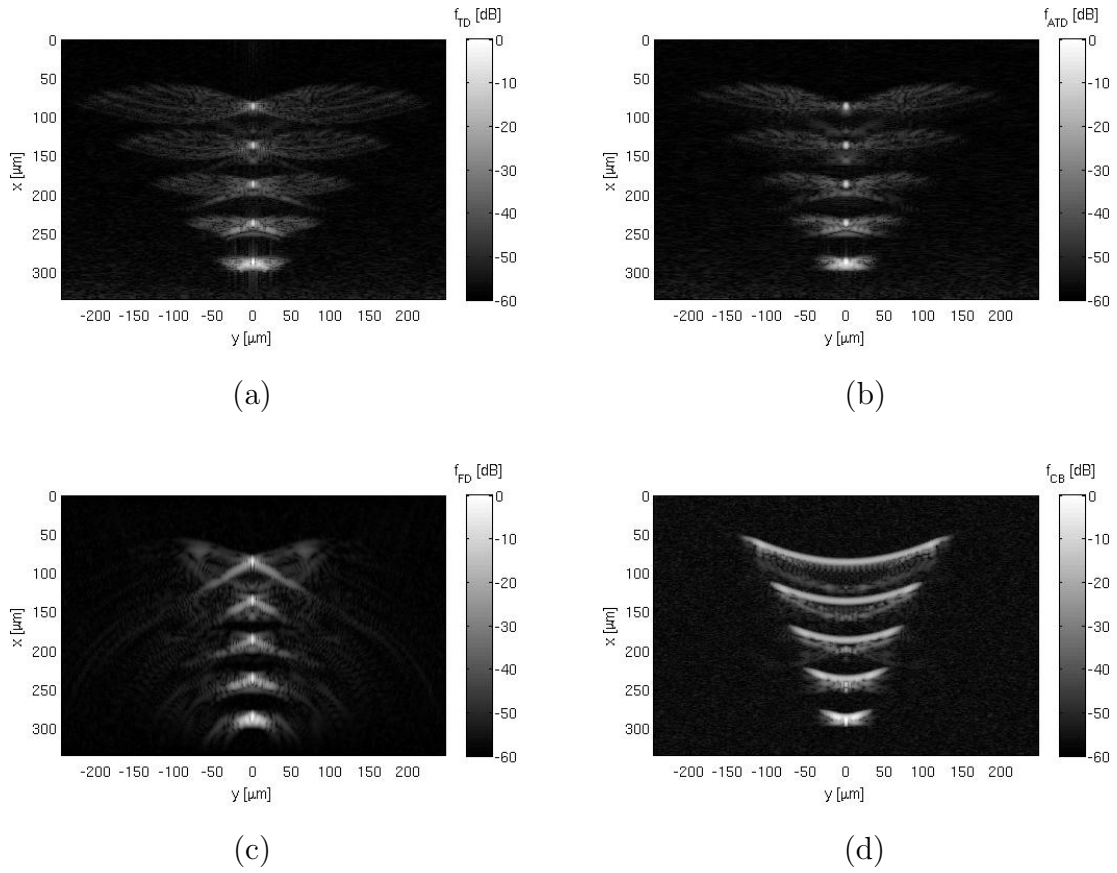
Figure 4.4: Images of five point scatterers placed before the focus reconstructed using the (a) TD-SAFT, (b) ATD-SAFT (c) FD-SAFT, (d) conventional B-mode imaging with a 10 dB SNR.

(a)

(b)

(c)

(d)

(e)
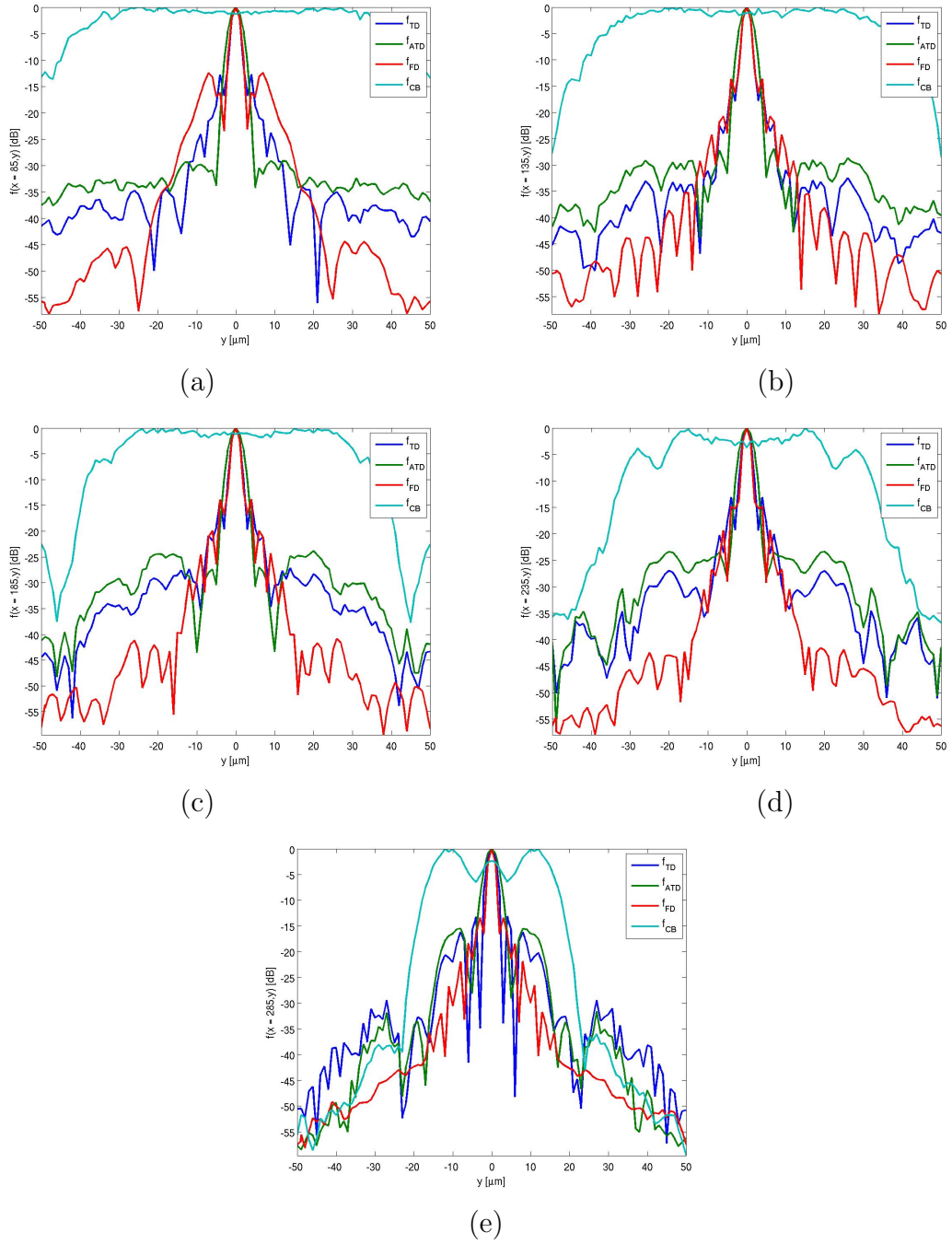
Figure 4.5: The lateral profiles of the images with an SNR of 10 dB at (a) 85 μm, (b) 135 μm, (c) 185 μm, (d) 235 μm, (e) 285 μm.

b) All Scatterers After the Focus

The reconstructed images of the five point scatterers placed after the focal spot from 385 μm to 535 μm with a step-size of 50 μm are provided in figure 4.6. The reconstruction techniques used in figure 4.6 (a)-(d) are TD-SAFT, ATD-SAFT, FD-SAFT and conventional B-mode imaging method, respectively. The lateral profiles of these images at the location of the scatterers are shown in figure 4.7.

(a)   (b)

(c)   (d)
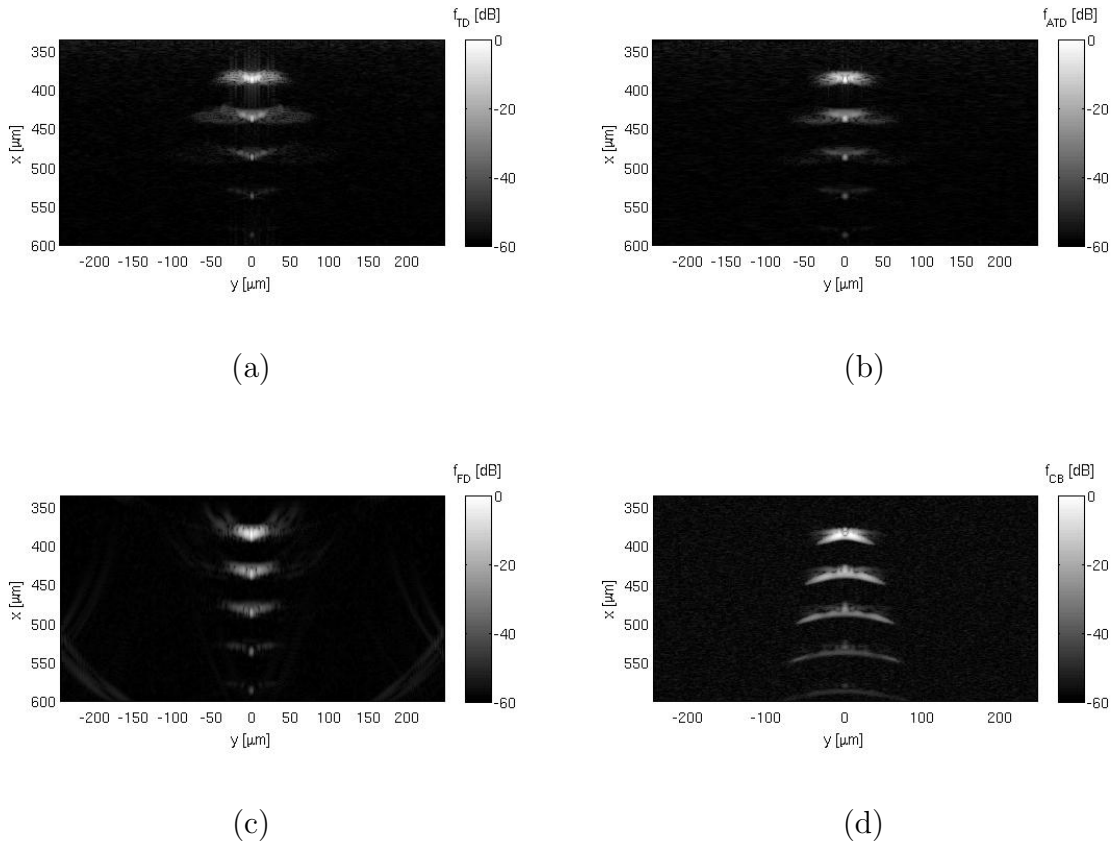
Figure 4.6: Images of five point scatterers placed after the focus reconstructed using the (a) TD-SAFT, (b) ATD-SAFT (c) FD-SAFT, (d) conventional B-mode imaging with a 10 dB SNR.

(a)

(b)

(c)

(d)

(e)
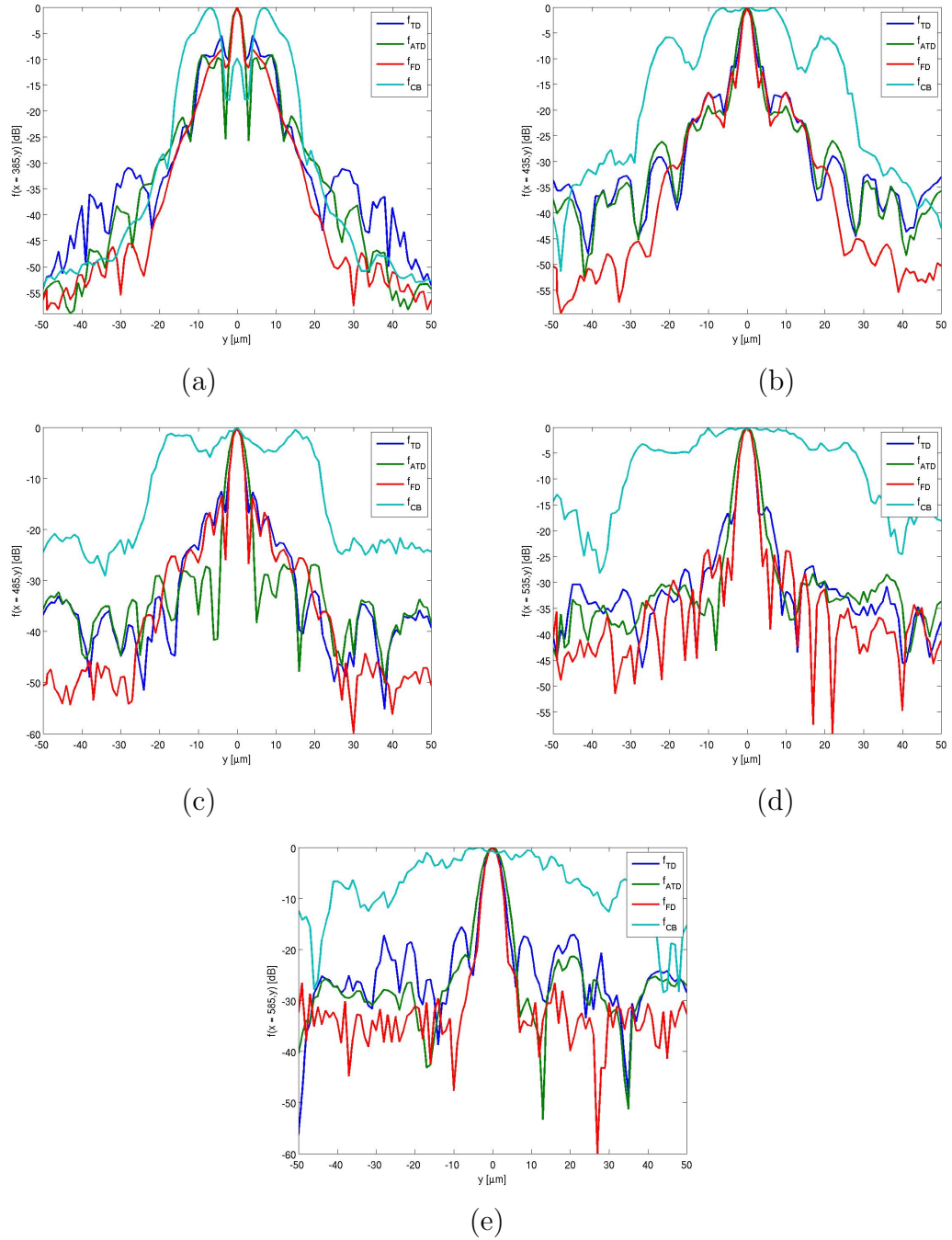
Figure 4.7: The lateral profiles of the images with an SNR of 10 dB at (a) 385 μm, (b) 435 μm, (c) 485 μm, (d) 535 μm, (e) 585 μm.

c) Quantification of the Image Quality

The FWHM value of the point spread function at the location of scatterers was used to evaluate the SAFT algorithms in comparison to the conventional B-mode imaging. Figure 4.8 (a) shows the lateral resolutions obtained from the conventional B-mode image and the SAFT algorithms used to reconstruct images shown in figures 4.4 and 4.6 at the location of all scatterers. For a better visualization of the FWHM values obtained from SAFT, the FWHM values obtained from the SAFT reconstructed images without including the FWHM obtained in the conventional B-mode imaging are shown in figure 4.8 (b). Percent reduction in FWHM values, r_{FWHM}, calculated from equation 2.8 are shown in figure 4.8 (c). Figure 4.8 (d) provides the first side lobe levels, f_{SL}, of the lateral profiles at the location of all scatterers in the reconstructed images.
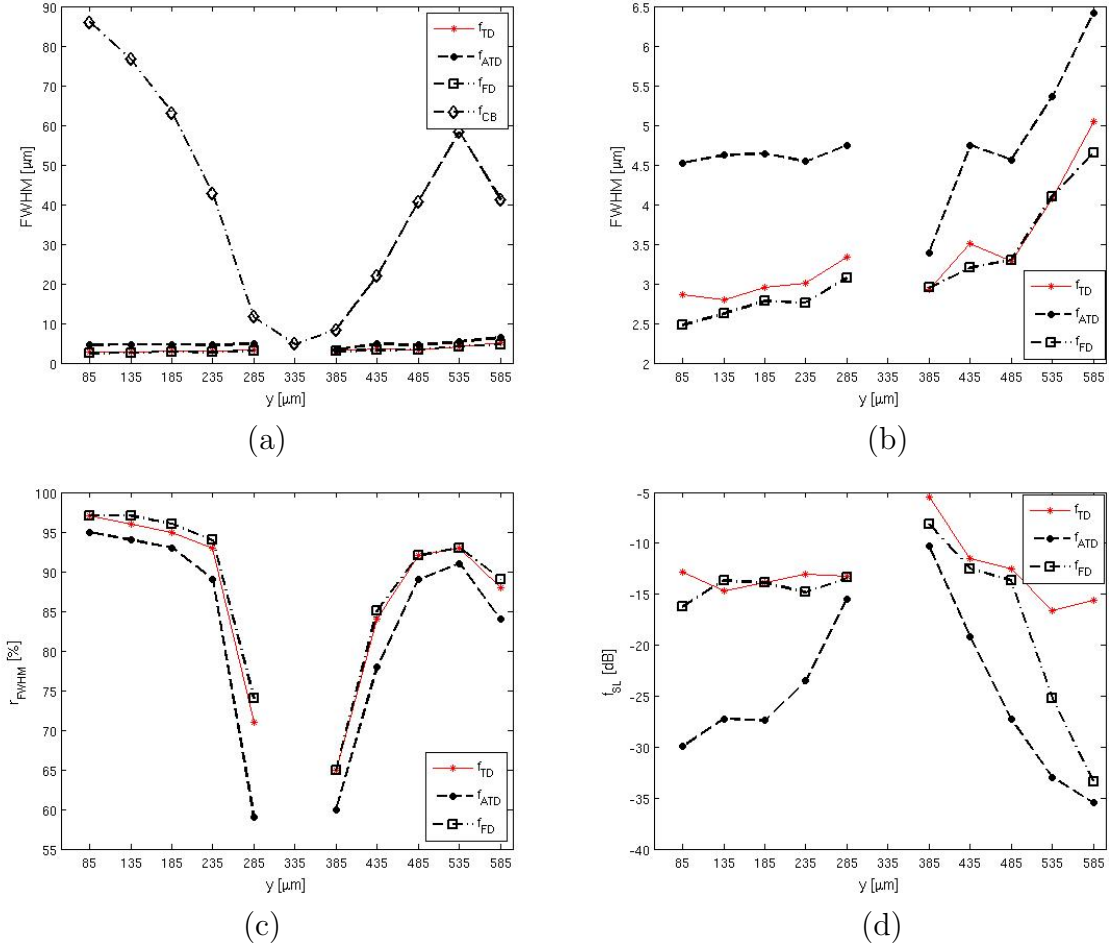
Figure 4.8: Comparison of the resolution and side lobes of SAFT reconstructed images with a 10 dB SNR. (a) shows the FWHM based on conventional B-mode imaging as well as the reconstructed algorithms, (b) shows the FWHM from the reconstructed algorithms only, (c) and (d) show the r_{FWHM} and f_{SL}, respectively, for all the scatterer locations.

4.1.2.2   Image Reconstruction With 5 dB SNR

a) All Scatterers Before the Focus

The reconstructed images from the simulated RF data with an SNR of 5 dB of scatterers placed before the focus using TD-SAFT, ATD-SAFT, FD-SAFT and conventional B-mode imaging method are shown in figure 4.9 (a)-(d), respectively. The lateral profiles of the images with an SNR of 5 dB at the location of the scatterers placed before the focus are shown in figure 4.10.

(a)   (b)

(c)   (d)
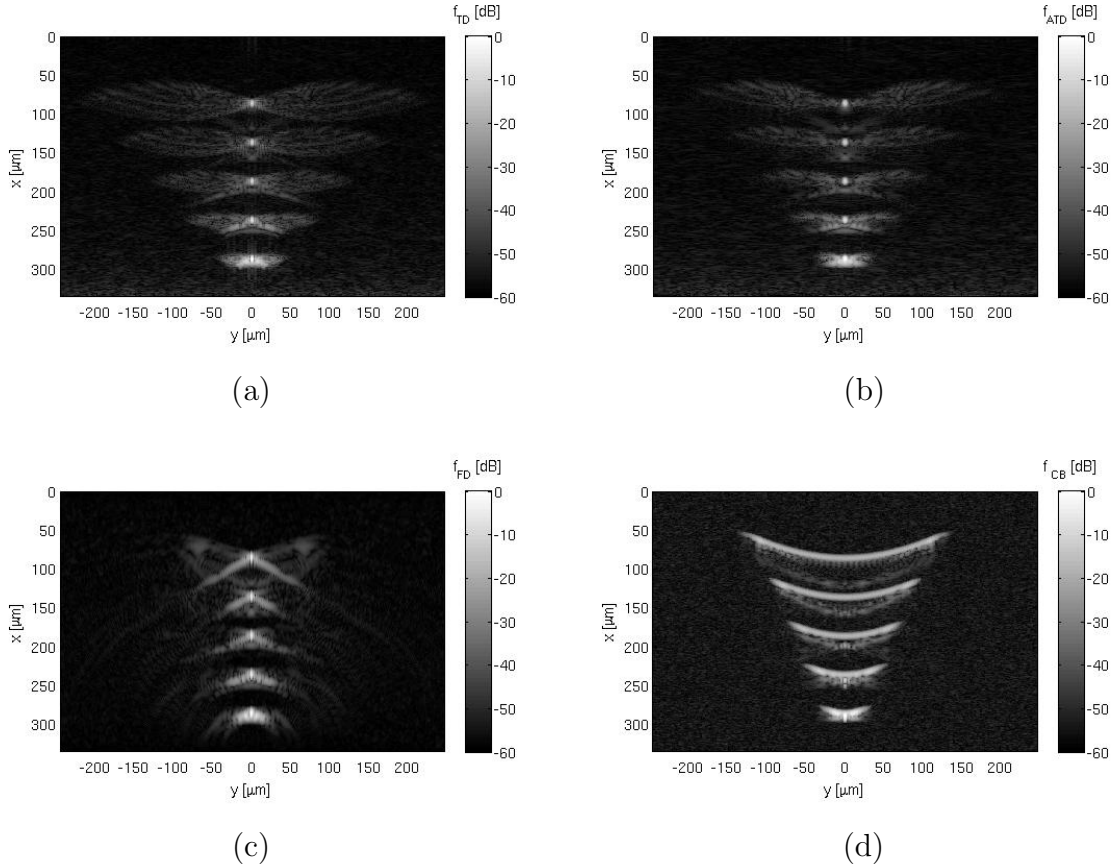
Figure 4.9: Images of five point scatterers placed before the focus reconstructed using the (a) TD-SAFT, (b) ATD-SAFT (c) FD-SAFT, (d) conventional B-mode imaging with a 5 dB SNR.

(a)

(b)

(c)

(d)

(e)
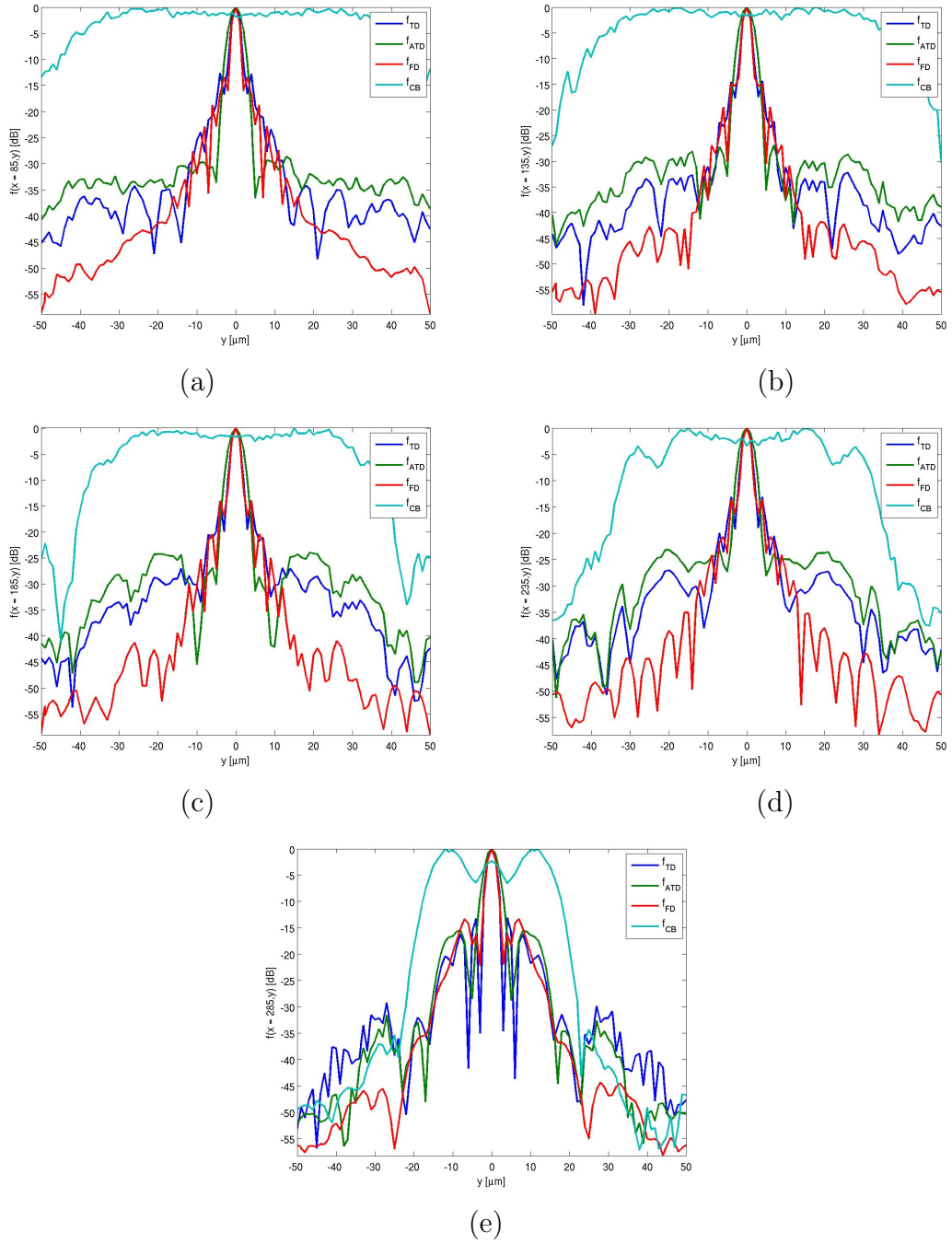
Figure 4.10:   The lateral profiles of the images with an SNR of 5 dB at (a) 85 μm, (b) 135 μm, (c) 185 μm, (d) 235 μm, (e) 285 μm.

b) All Scatterers After the Focus

The reconstructed images from the simulated RF data with an SNR of 5 dB of scatterers placed after the focus using TD-SAFT, ATD-SAFT, FD-SAFT and conventional B-mode imaging method are shown in figure 4.11 (a)-(d), respectively. The lateral profiles of the images with an SNR of 5 dB at the location of the scatterers placed after the focus are shown in figure 4.12.


(a)

(b)

(c)

(d)
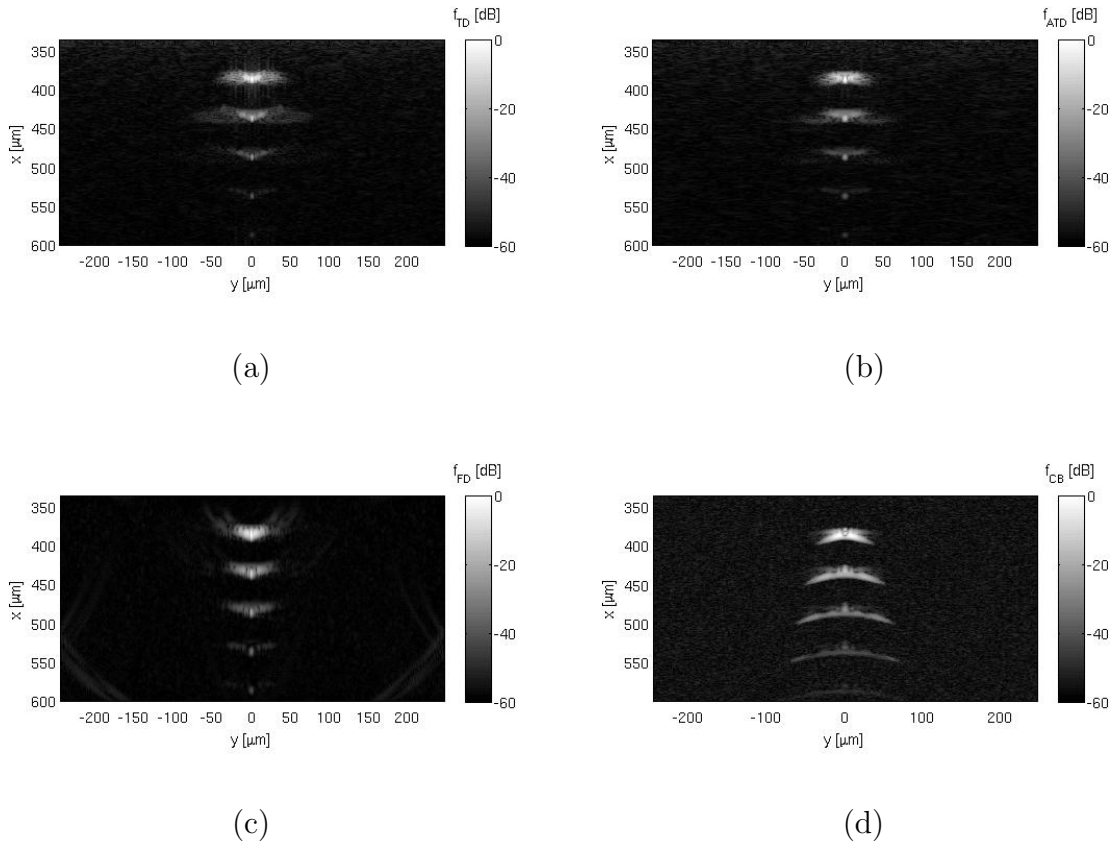
Figure 4.11: Images of five point scatterers placed after the focus reconstructed using the (a) TD-SAFT, (b) ATD-SAFT (c) FD-SAFT, (d) conventional B-mode imaging with a 5 dB SNR.

(a)

(b)

(c)

(d)

(e)
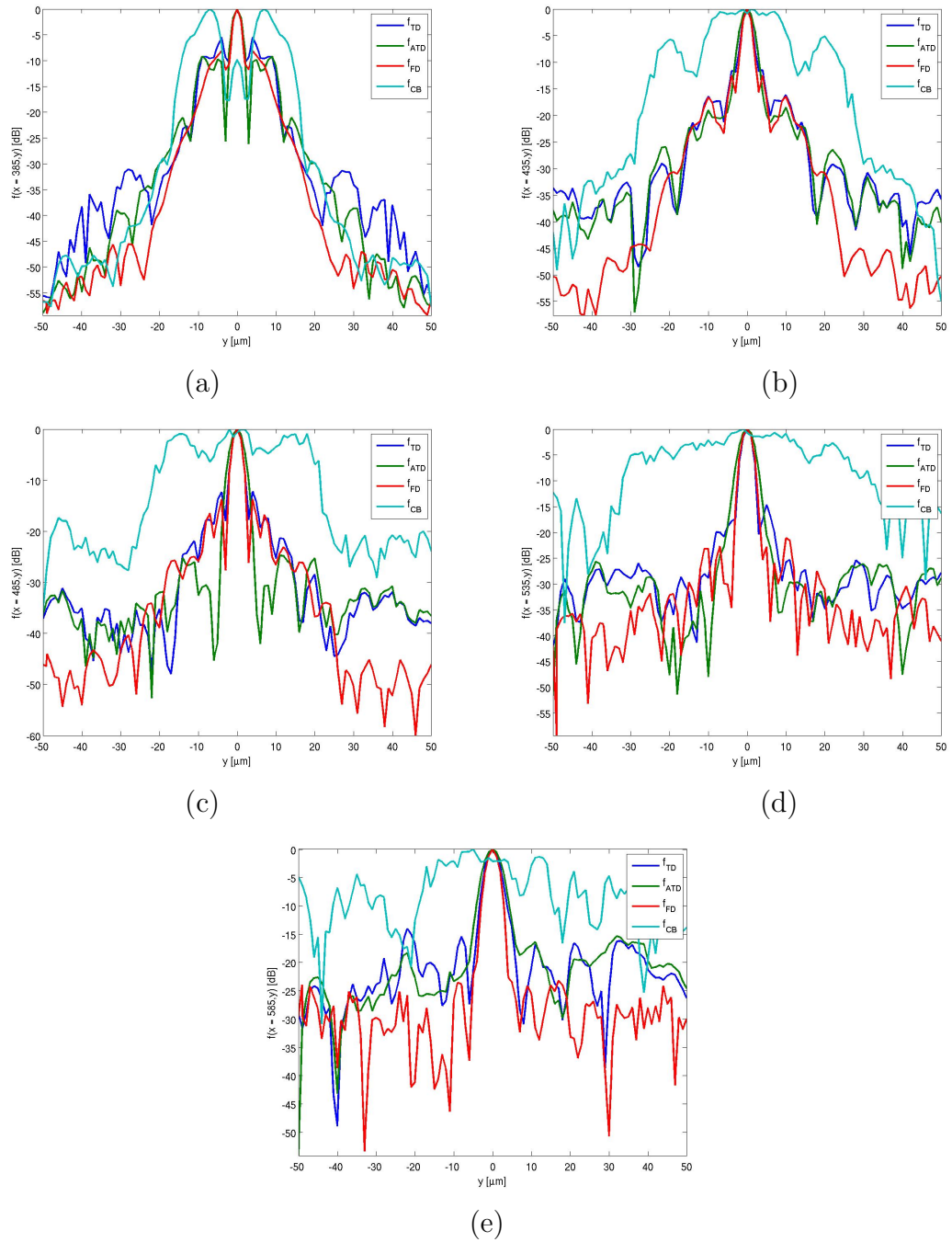
Figure 4.12: The lateral profiles of the images with an SNR of 5 dB at (a) 385 μm, (b) 435 μm, (c) 485 μm, (d) 535 μm, (e) 585 μm.

c) Quantification of the Image Quality

Figure 4.13 (a) shows the lateral resolutions obtained from the conventional B-mode image and the SAFT algorithms used to reconstruct images shown in figures 4.9 and 4.11 at the location of all scatterers. The FWHM values obtained from the SAFT reconstructed images without including the FWHM obtained in the conventional B-mode imaging are shown in figure 4.13 (b). Percent reduction in FWHM values, r_{FWHM}, calculated from equation 2.8 are shown in figure 4.13 (c). Figure 4.13 (d) provides the first side lobe levels of the lateral profiles at the location of all scatterers reconstructed images.
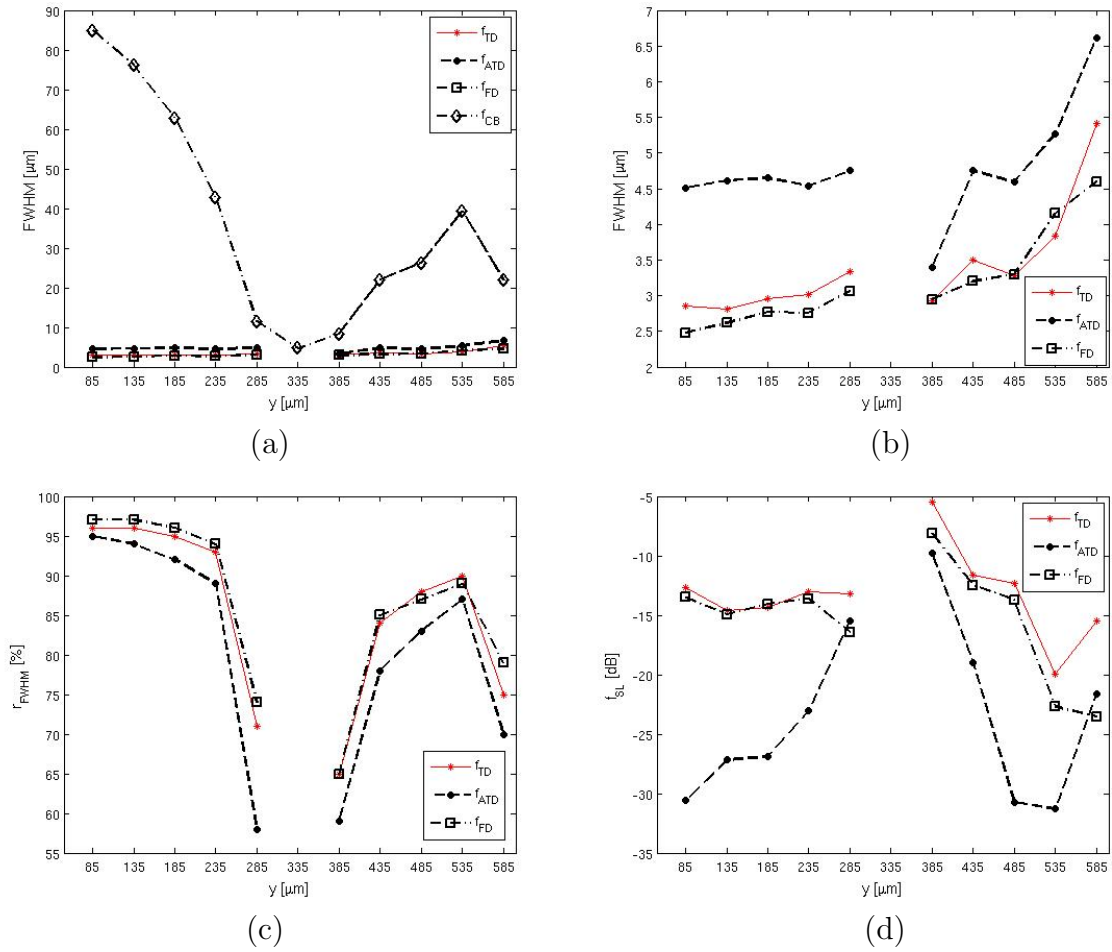
Figure 4.13: Comparison of the resolution and side lobes of SAFT reconstructed images at 5 dB. (a) shows the FWHM based on conventional B-mode imaging as well as the reconstructed algorithms, (b) shows the FWHM from the reconstructed algorithms only, (c) and (d) show the r_{FWHM}, and f_{SL}, respectively, for all the scatterer locations.

4.2 Experiments

In this section the reconstructed images of experimental data, as described in section 3.4, are presented. The results of the first set of experiments performed by acquiring data from a phantom with a sparse arrangement of 2 μm carbon beads are provided in section 4.2.1. In section 4.2.2, the results acquired from two carbon beads placed close to each other are presented. Section 4.2.3 provides the images of a spheroid.

4.2.1 Images of a Single Bead

Figure 4.14 shows the image of a 2 μm bead placed at 50 μm before the focus. Figures 4.15- 4.18 show the reconstructed images of a 2 μm bead placed at 15 μm, 30 μm, 50 μm, and 75 μm after the focus, respectively.

(a)

(b)

(e)

(f)
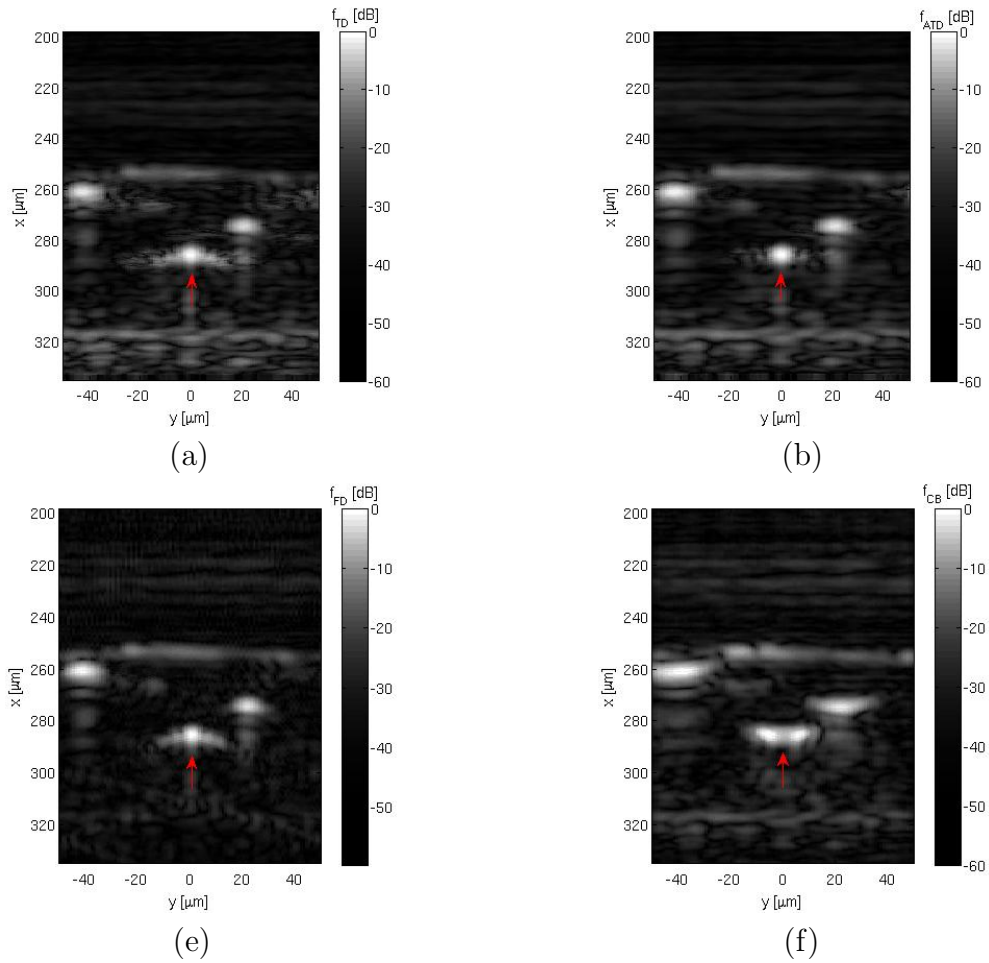
Figure 4.14: Images of a 2 μm bead placed at 50 μm before the focus reconstructed using (a) TD-SAFT, (b) ATD-SAFT, (c) FD-SAFT, and (d) conventional B-mode imaging, respectively.
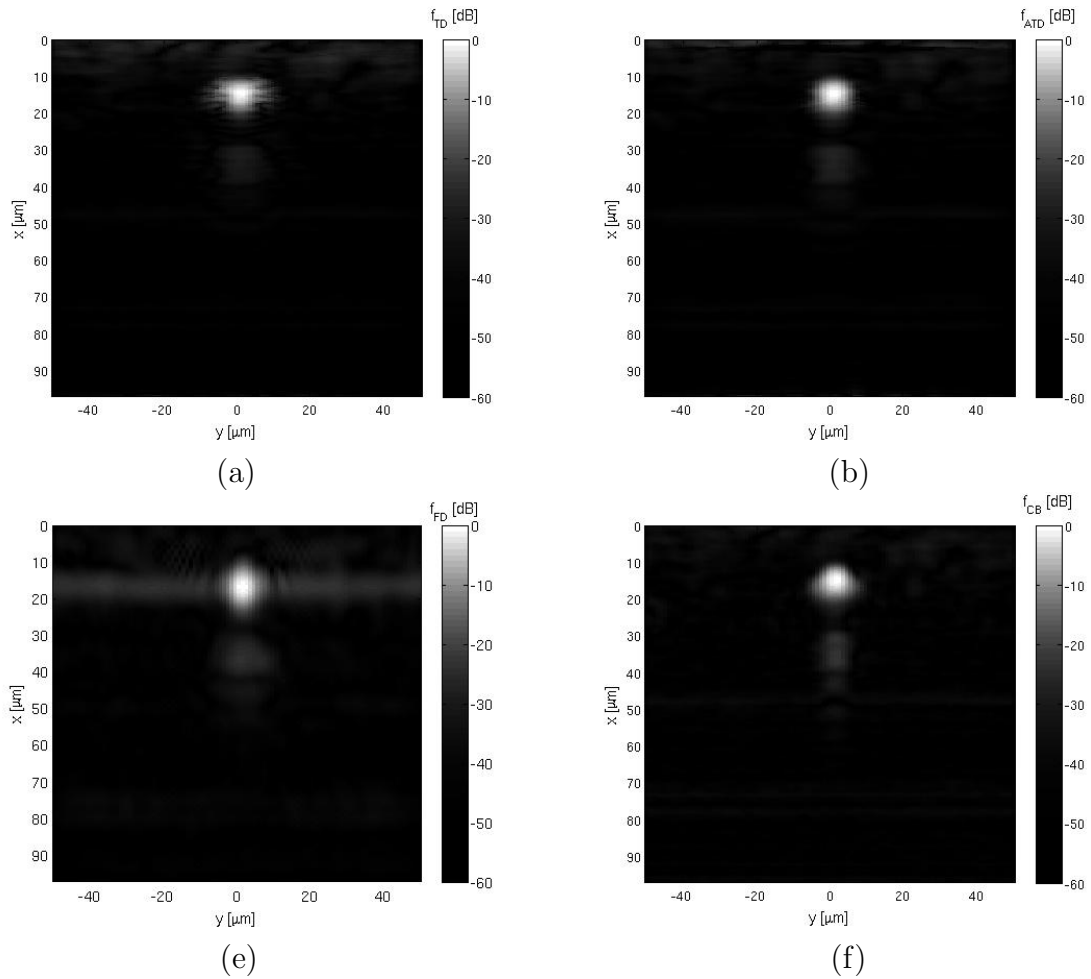
Figure 4.15: Images of a 2 μm bead placed at 15 μm after the focus reconstructed using (a) TD-SAFT, (b) ATD-SAFT, (c) FD-SAFT, and (d) conventional B-mode imaging, respectively.
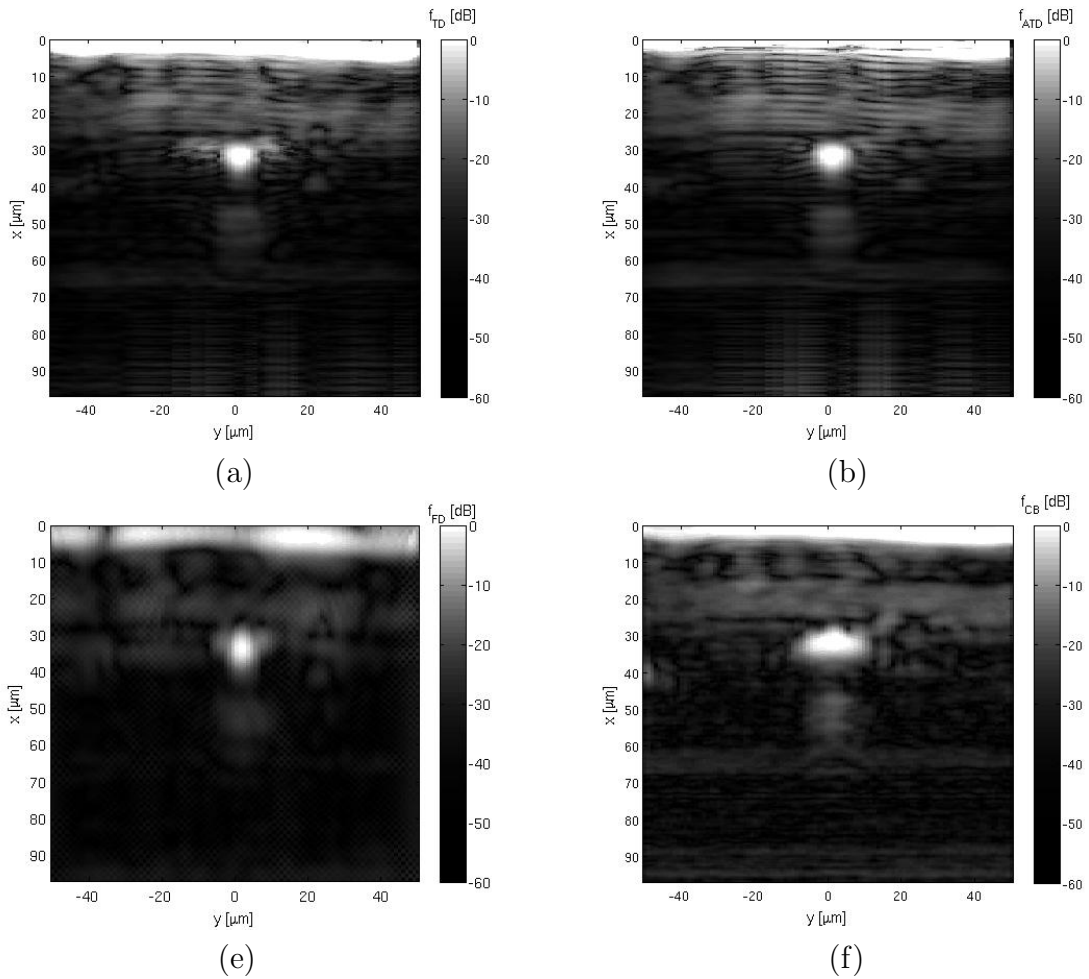
Figure 4.16: Images of a 2 μm bead placed at 30 μm after the focus reconstructed using (a) TD-SAFT, (b) ATD-SAFT, (c) FD-SAFT, and (d) conventional B-mode imaging, respectively.

(a)   (b)

(e)   (f)
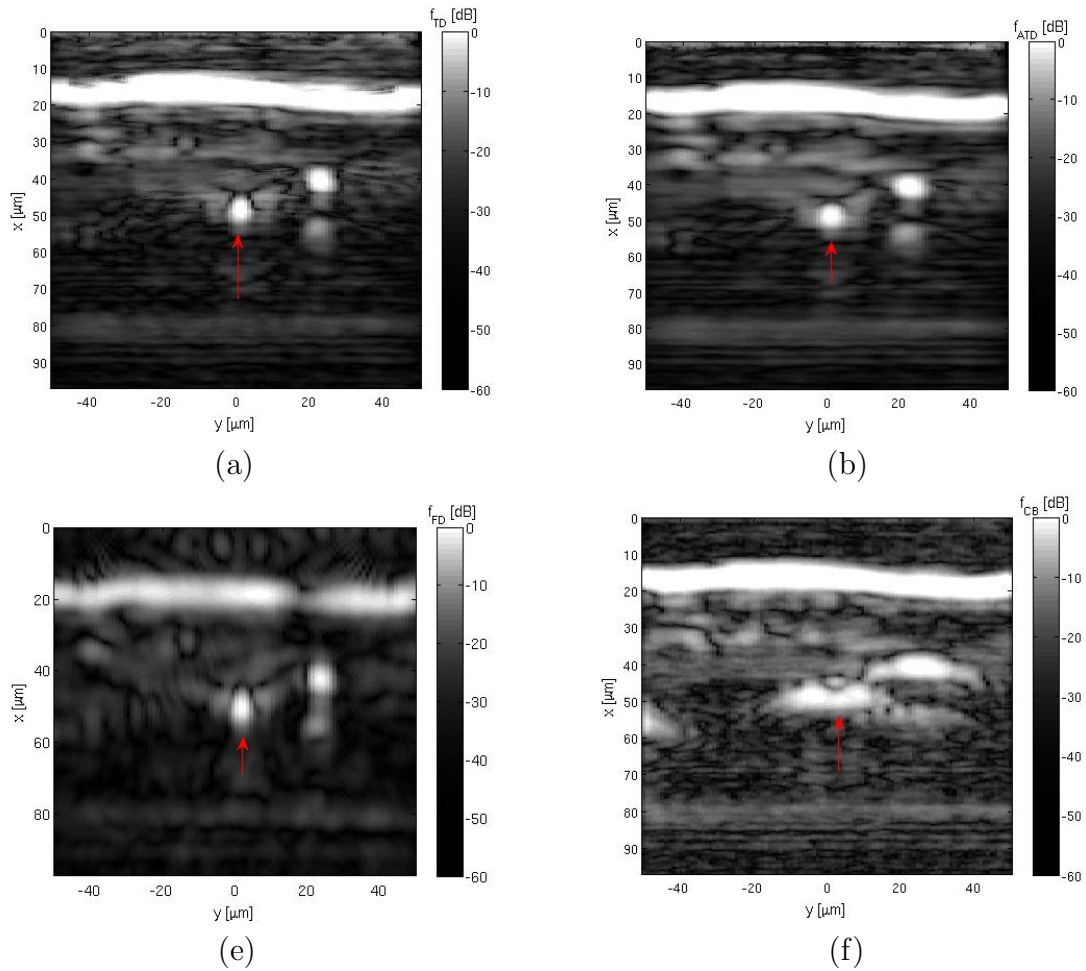
Figure 4.17: Images of a 2 μm bead placed at 50 μm after the focus reconstructed using (a) TD-SAFT, (b) ATD-SAFT, (c) FD-SAFT, and (d) conventional B-mode imaging, respectively. Another bead of an unkown size is also visible.
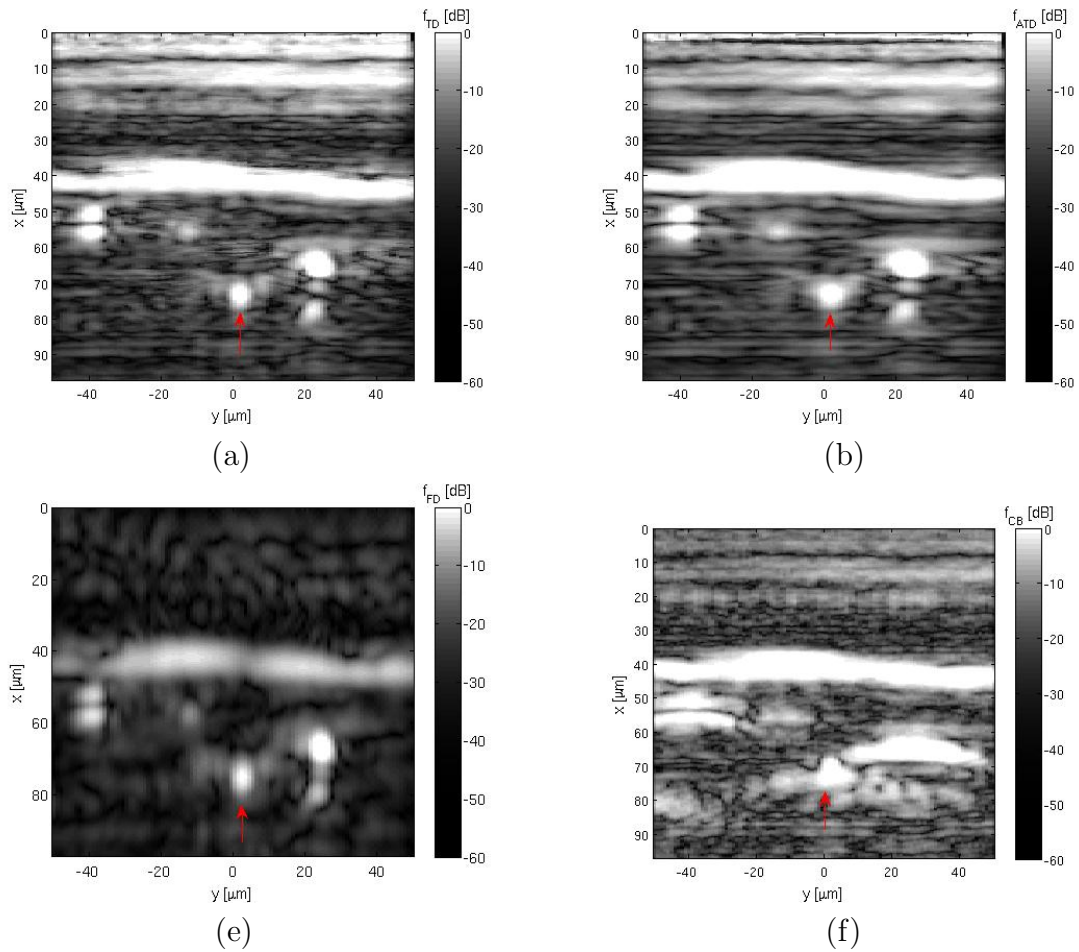
Figure 4.18: Images of a 2 μm bead placed at 75 μm after the focus reconstructed using (a) TD-SAFT, (b) ATD-SAFT, (c) FD-SAFT, and (d) conventional B-mode imaging, respectively. Another bead of an unkown size is also visible.

4.2.2 Resolvability of Two Closely Spaced Beads

The optical image of two carbon beads placed close to each other is shown in figure 4.19 and the conventional B-mode image of the same beads placed at the focus of the transducer is shown in figure 4.20. Figures 4.21- 4.23 show the reconstructed images of two carbon beads placed close to each other at 15 μm, 30 μm, and 50 μm after the focus, respectively. Image reconstruction in all of these figures were done using (a) TD-SAFT, (b) ATD-SAFT, (c) FD-SAFT, and (d) conventional B-mode imaging, respectively.
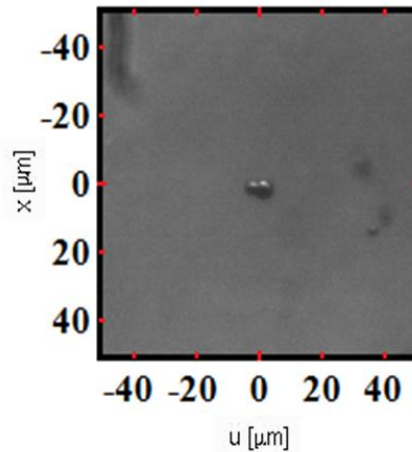
Figure 4.19: The optical image of two closely positioned micro-beads.
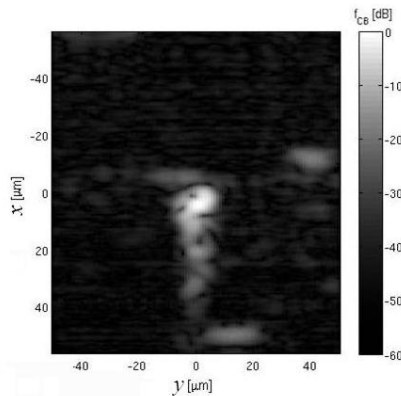
Figure 4.20: The conventional B-mode image of two micro-beads at the focus.

(a)

(b)

(c)

(d)
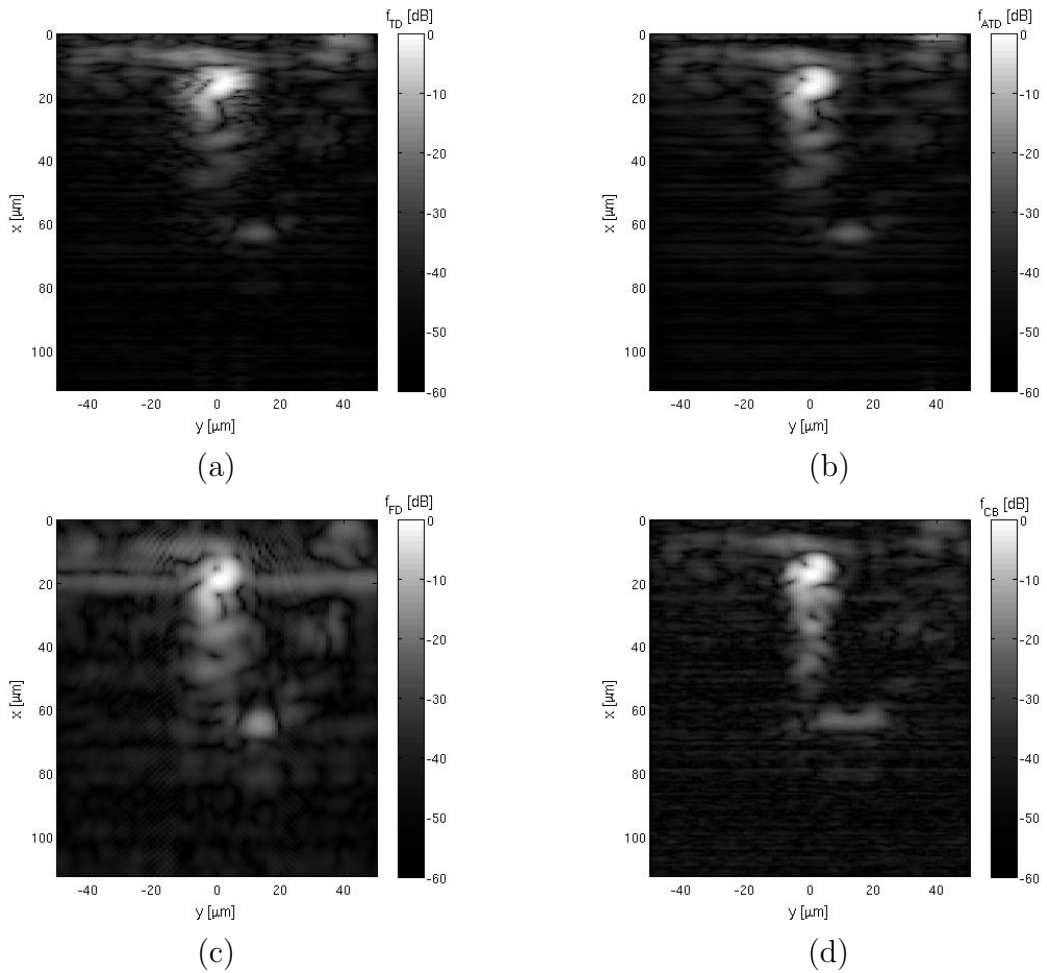
Figure 4.21: Images of two micro-beads at 15 μm after the focus reconstructed using (a) TD-SAFT, (b) ATD-SAFT, (c) FD-SAFT, and (d) conventional B-mode imaging, respectively.

(a)

(b)

(e)

(f)
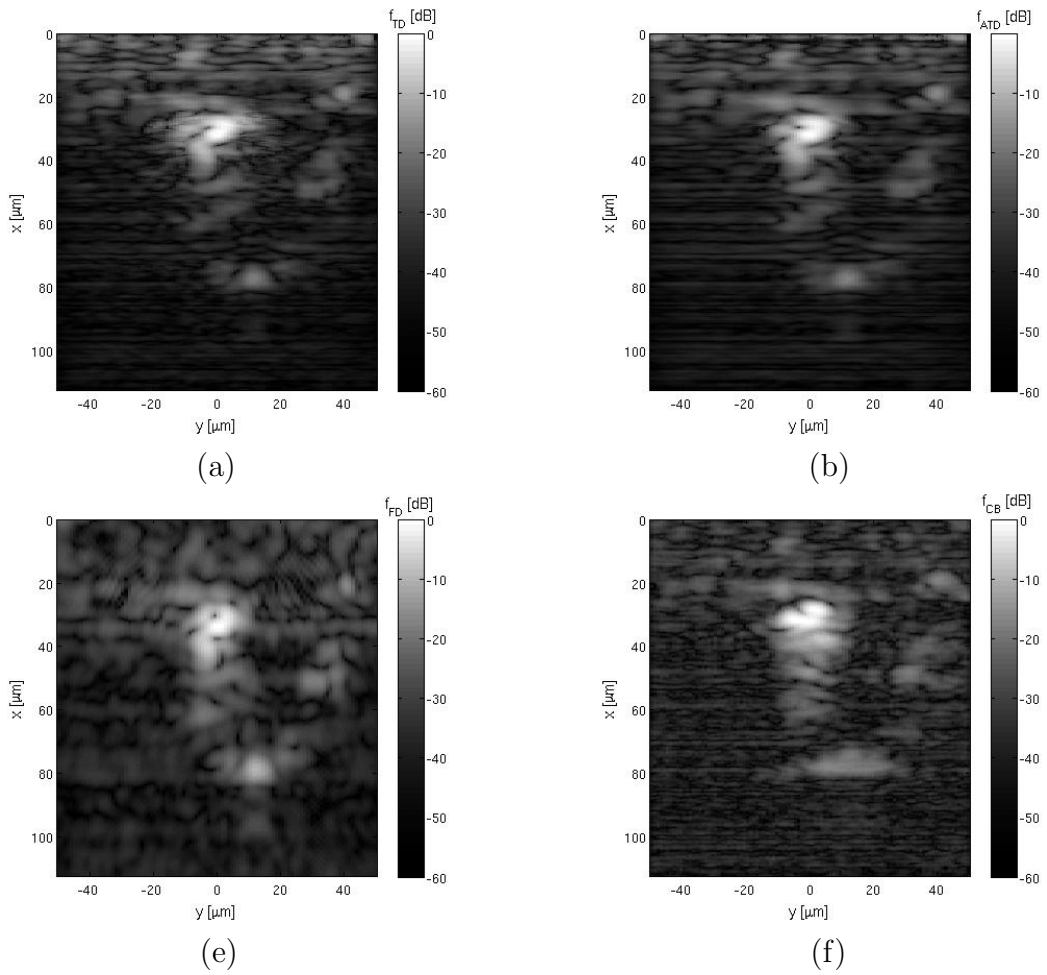
Figure 4.22: Images of two micro-beads at 30 μm after the focus reconstructed using (a) TD-SAFT, (b) ATD-SAFT, (c) FD-SAFT, and (d) conventional B-mode imaging, respectively.

(a)

(b)

(e)

(f)
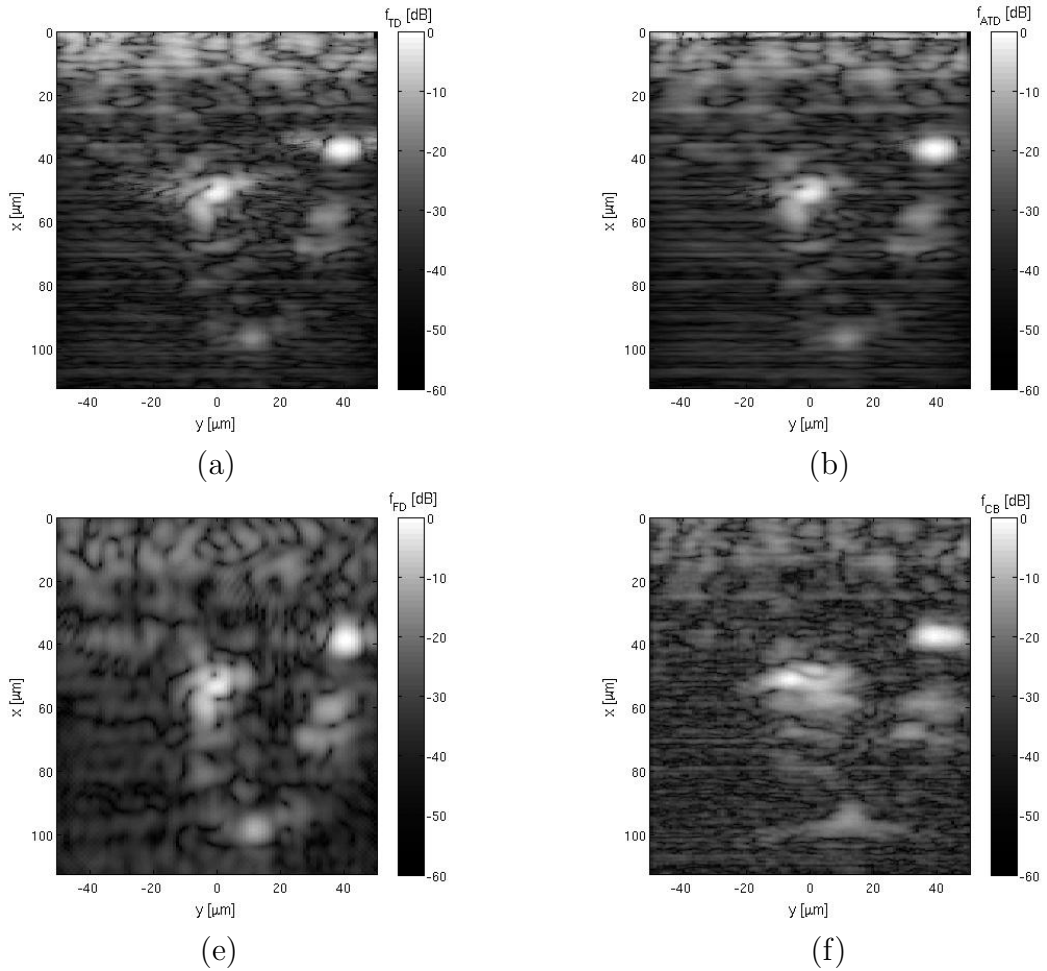
Figure 4.23: Images of two micro-beads at 50 μm after the focus reconstructed using (a) TD-SAFT, (b) ATD-SAFT, (c) FD-SAFT, and (d) conventional B-mode imaging, respectively.

### 4.2.3   Images of a Spheroid

Figure 4.24 (a) shows the B-mode image of the spheroid when the focus was placed at 60 μm above the substrate with Wiener filtering. The image is contaminated with artifacts, which appeared as horizontal lines, which are not removed by the Wiener filter. In order to improve the image quality, the average value of the rows of the RF matrix was subtracted from the RF matrix values of each row. This method is referred to as the row average subtraction in this thesis. The obtained image is shown in figure 4.24 (b) showing a reduction of the artifacts. As a result, before processing the data obtained from the spheroid, Wiener filtering and row average subtraction were performed.

Figure 4.25 (a)-(c) show the reconstructed image of the spheroid using TD-SAFT, ATD-SAFT and FD-SAF, respectively, when the focus of the transducer was placed at 60 μm above the substrate.

Figure 4.26 (a) and (b) show the conventional B-mode image of the spheroid when the focus was placed 115 μm above the substrate without and with row average subtraction, respectively. Figure 4.27 (a)-(c) show the reconstructed image of the spheroid using TD-SAFT, ATD-SAFT and FD-SAF, respectively, when the focus of the transducer was placed at 115 μm above the substrate.
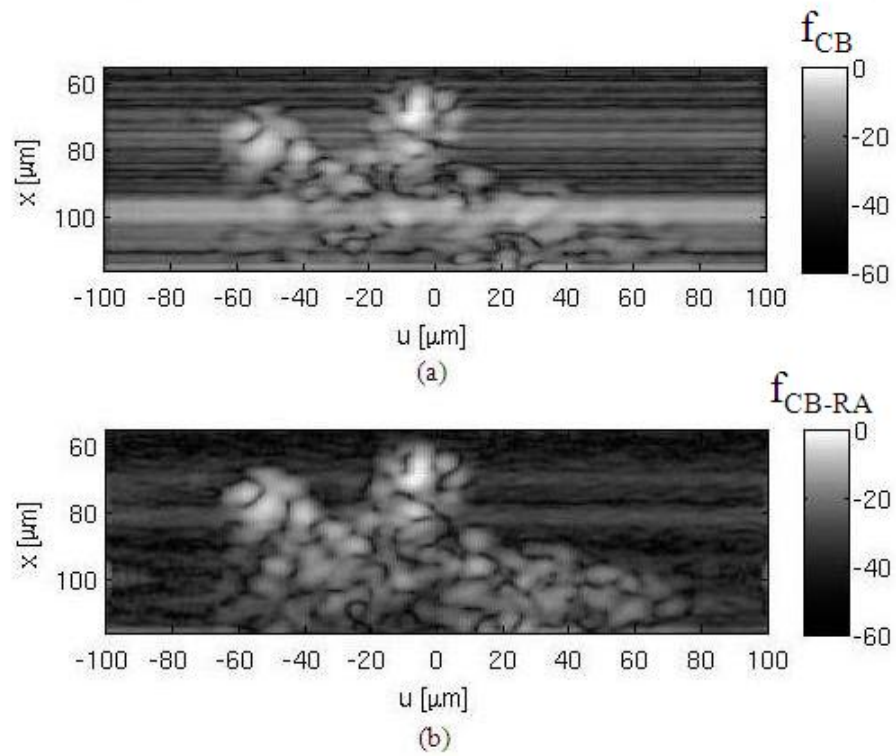
Figure 4.24: Conventional B-mode image of the spheroid when the focus was placed at 60 μm above the substrate (a) without row average subtraction, and (b) with row average subtraction.
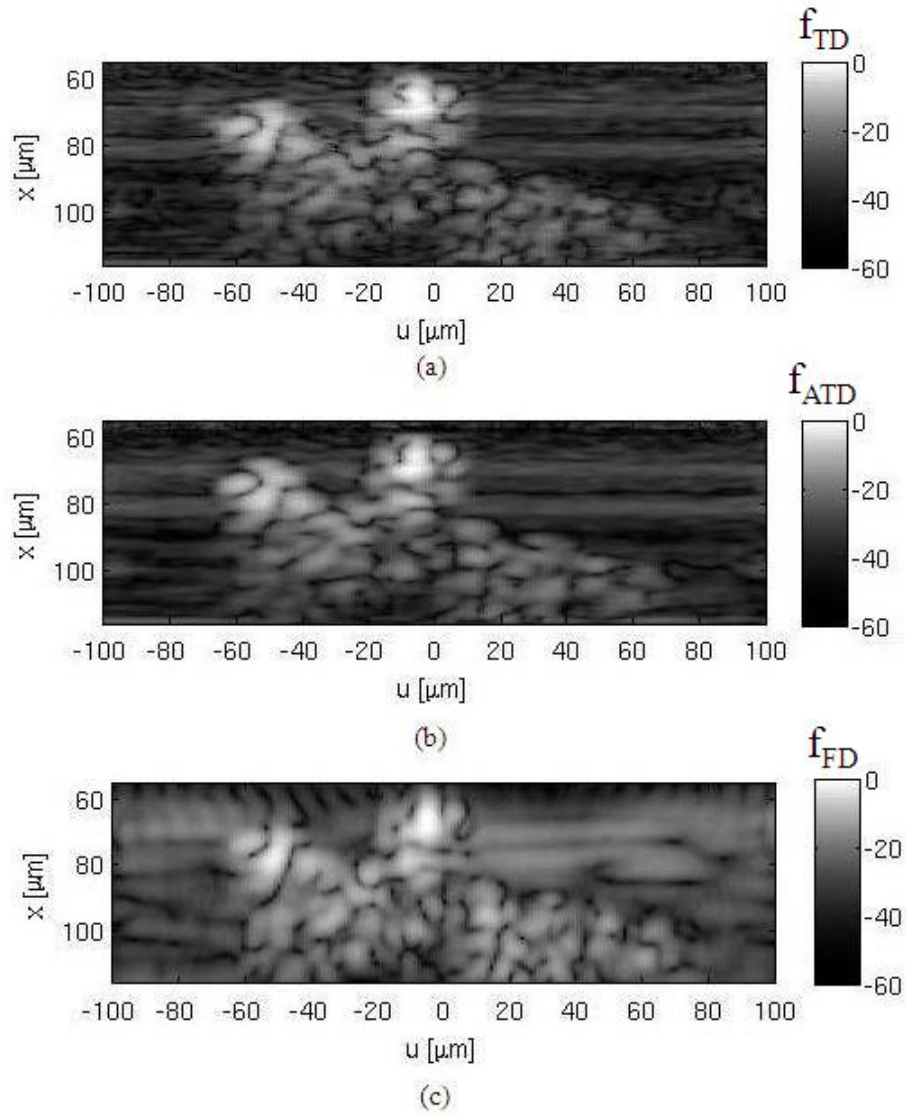
Figure 4.25: Reconstructed images of the spheroid with the focus at 60μm above the substrate using (a) TD-SAFT, (b) ATD-SAFT, and (c) FD-SAFT.
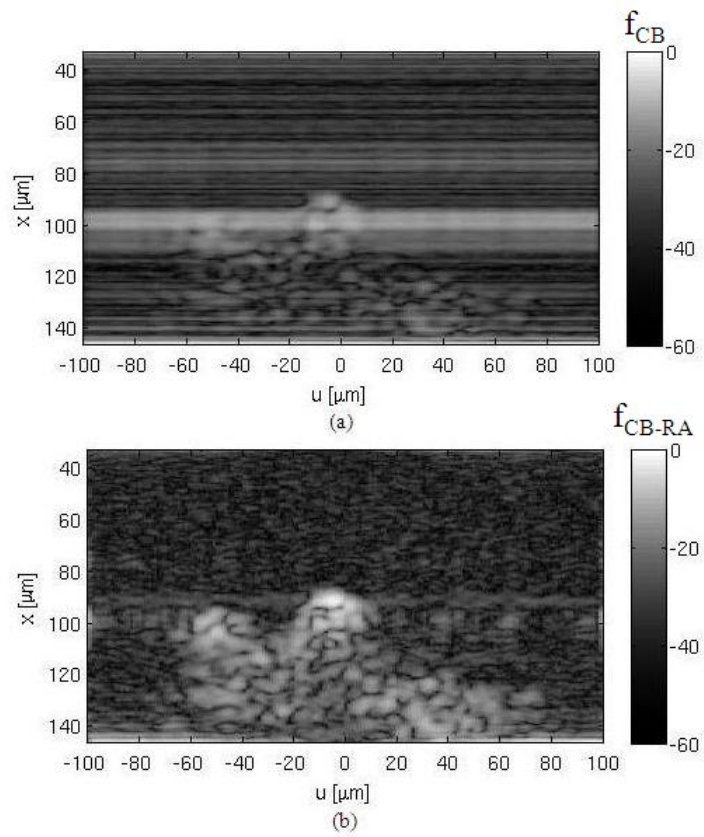
Figure 4.26: Conventional B-mode image of the spheroid when the focus was placed at 115μm above the substrate (a) without row average subtraction, and (b) with row average subtraction.
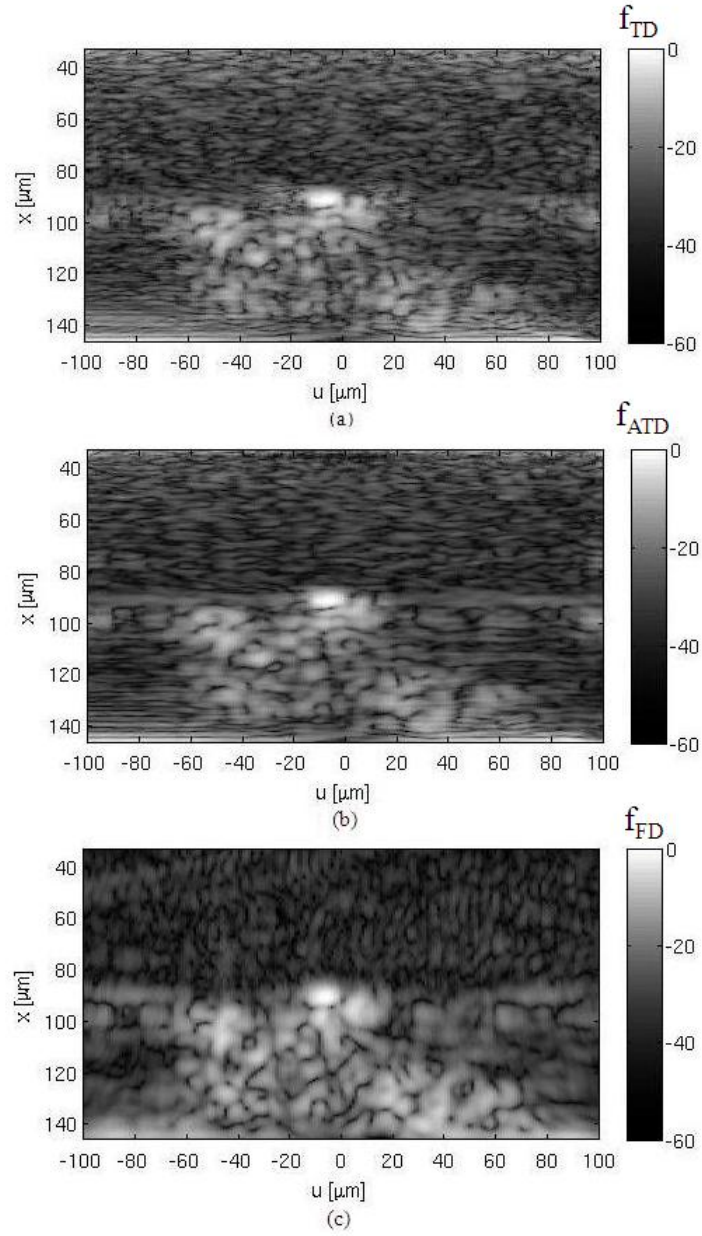
Figure 4.27: Reconstructed images of the spheroid with the focus at 115μm above the substrate using (a) TD-SAFT, (b) ATD-SAFT, and (c) FD-SAFT.

Chapter 5

Discussion

5.1 Implementation Verification

The reconstruction images of a scatterer placed 40 mm away from a piston transducer using the TD-SAFT and FD-SAFT are shown in section 4.1.1. The simulation in [22] was replicated and the TD-SAFT implementation was used to reconstruct the image of the scatterer from the simulated RF data. The reconstructed image of the scatterer presented in [22], as well as the obtained image in this work were shown in figure 4.1(a) and (b), respectively. The similarity between the images the TD-SAFT implementation verifies the TD-SAFT implementation. The small differences in the images could be due to the possible differences between the impulse response used in the simulations and that used in section 4.1.1. The impulse response used in the simulations was reverse engineered by digitizing the image of the impulse response plot in [22], which may have affected the replication of the simulated RF data.

The reconstructed image of the scatterer using a modified FD-SAFT, which incorporates the diffraction effects of the transducer was provided in [22], and shown in figure 4.2 (a). The reconstructed image of the scatterer using FD-SAFT, assuming a point source and no diffraction effects was shown in figure 4.2 (b). The reconstructed images

of the scatterer with the FD-SAFT showed lower side lobes in comparison to the TD-SAFT reconstructed images. Figure 4.2 (a) had a better lateral and axial resolution in comparison to figure 4.2 (b). Therefore, there is room for improvement for the implemented FD-SAFT in order to increase the image quality by incorporating the diffraction effects of the transducer in the image reconstruction algorithms. However, incorporating the diffraction effects of the transducer in the FD-SAFT was not implemented in this thesis as the focus of this thesis was to complete the study of the performance of the implemented algorithms quantitatively in simulations and quantitatively in experiments.

5.2 Simulations Based on SASAM

It was shown in section 2.5.1 that as the synthetic focusing point at location $p(x, y)$ gets closer to the virtual source, the synthetic aperture length, L, gets smaller. Therefore, around the geometrical focal region of the transducer, the number of RF lines that can contribute to focusing in the TD-SAFT and ATD-SAFT decreases as the overlapping field at different scan positions is narrower in the areas closer to the virtual source. As a result, SAFT performs better in the regions away from the virtual source in comparison to the regions closer to the focus. In addition, images of scatterers placed at the focus of the transducer cannot be reconstructed in SAFT. Therefore, a dual-mode reconstruction could be developed, which uses the conventional B-mode imaging near the focus and SAFT away from the focus.

It is known that at frequencies used in acoustic microscopy, attenuation in a medium is high and as a result the acoustic wave cannot propagate deep in the medium limiting the maximum depth of a conventional B-mode image. This issue could be addressed by placing the focus after the region of interest and using SAFT to reconstruct an image of the ROI, since the RF data is less attenuated due to propagating over a shorter depth in comparison to the RF data acquired from regions passed the focus.

The effect of Wiener filtering in the conventional B-mode image obtained from simulated RF data of the SASAM system was investigated. As shown in figure 4.3 (b), the Wiener filter performed well in reducing the noise visible in figure 4.3 (a). As a result, Wiener filtering was performed before image reconstruction for all reconstructions from simulated and experimental scans.

The performance of different SAFT algorithms was evaluated by comparing the full width at half maximum as well as the side lobe level drop of the lateral profiles at the location of the scatterers obtained from different reconstruction techniques. A comparison of the FWHM results was done by calculating the reduction in the FWHM of SAFT reconstructed images with respect to the FWHM of the conventional B-mode images at each scatterer location. r_{FWHM} was calculated using equation (2.8). The details of the quantitative analysis of the SAFT performance using simulated data with 10 dB SNR and 5 dB SNR are provided in sections 5.2.1 and 5.2.2, respectively.

5.2.1 Scatterers Placed Before and After the Focus With an SNR of 10 dB

The conventional B-mode image as well as the SAFT reconstructed images from simulated data with an SNR of 10 dB of scatterers placed before and after the geometrical focus of the transducer are provided in figure 4.4 and 4.6, respectively. The lateral profiles at the location of scatterers for different reconstruction techniques are provided in figure 4.5 for the case with the scatterers placed before the focus and in 4.7 for the case with the scatterers placed after the focus.

The FWHM values at the location of all the scatterers for the conventional B-mode image as well as the SAFT reconstructed images are provided in figure 4.8 (a). It was observed in figure 4.8 (a) that the SAFT algorithms performed much better than the conventional B-mode image in providing a smaller FWHM. The FWHM obtained from

the conventional B-mode image of a scatterer placed at the focus of the transducer is also provided in figure 4.8 (a) in order to compare the SAFT performance throughout the region of interest with the conventional B-mode image of highest lateral resolution, which is obtained at the geometrical focus of the transducer.

It was observed that all the SAFT algorithms used to reconstruct images in figure 4.4 and 4.6 provided smaller or similar FWHM values in comparison to the FWHM obtained from the conventional B-mode of a scatterer at the focus.

In figure 4.8 (b), the FWHM values at the location of scatterers for the SAFT reconstructed images are provided, without including those of the conventional B-mode images for better visualization. For the scatterers placed either before or after the focus, it was observed that the FD-SAFT performed better than the TD-SAFT and ATD-SAFT. The TD-SAFT resulted in slightly lower FWHM values in comparison to ATD-SAFT. This result was expected, as it is known that apodization lowers the lateral resolution, i.e. increases the FWHM, in ultrasound imaging.

Figure 4.8 (c) shows the percent reduction in the FWHM values of SAFT algorithms in comparison to the conventional B-mode image at each scatterer location. As shown in the figure, the r_{FWHM} increases as the distance of the scatterers from the virtual source increases. However, there is an exception at 585 μm, where r_{FWHM} is less than its preceding location's value, at 535 μm. The reason for this exception is that the FWHM value of the conventional B-mode image is better at 585 μm than 535 μm. The lateral profiles of the conventional B-mode images of scatterers at 535 μm and 585 μm, provided in figure 4.7 (d) and (e), respectively, illustrate that these lateral plots are very noisy. Due to the low SNR at such far locations from the focus, it is difficult to distinguish noise from the signal. Therefore, it is possible that the FWHM value at 585 μm is not a true value of the FWHM at that location.

The side lobe values of the lateral profiles at the scatterers' locations are shown in figure 4.8 (d). ATD-SAFT provided the lowest side lobe levels. For the scatterers placed

before the focus, FD-SAFT and TD-SAFT provided similar f_{SL} values. However, in the case of scatterers placed after the focus, the FD-SAFT performed better than TD-SAFT in providing lower f_{SL} values.

In short, base on figure 4.8, it could be concluded that FD-SAFT and TD-SAFT provide similar FWHM values, which are better than those of the ATD-SAFT. However, the ATD-SAFT provides the lowest side lobe levels at all depths.

5.2.2 Scatterers Placed Before and After the Focus With an SNR of 5 dB

The conventional B-mode image as well as the SAFT reconstructed images obtained from simulated data with an SNR of 5 dB for scatterers placed before and after the focus are shown in figure 4.9 and 4.11, respectively. Figure 4.10 shows the lateral profiles of the images of scatterers placed before the focus and figure 4.12 shows the lateral profiles of the images of scatterers placed after the focus.

Figure 4.13 (a) shows the FWHM values at the location of all the scatterers for the conventional B-mode image as well as the SAFT reconstructed images based on the data with an SNR of 5 dB. Similar to the results from the 10 dB data, the SAFT algorithms performed much better than the conventional B-mode image in providing smaller FWHM values, as shown in figure 4.13 (a). Similar results as those discussed in section 5.2.1 for the data with an SNR of 10 dB were obtained for the images obtained from the simulated data with an SNR of 5 dB. It was observed that all the SAFT algorithms used to reconstruct images in figure 4.9 and 4.11 provided smaller FWHM values than those obtained from the conventional B-mode images at the location of the scatterers. Additionally, the FWHM values obtained from SAFT reconstructed images were smaller than or equal to the FWHM of a scatter placed at the focus obtained from the conventional B-mode image. It was noted that the FWHM values obtained from the

conventional B-mode images of scatterers placed after the focus, decreased significantly after 435 μm in comparison to the FWHM values of the conventional B-mode image at the same scatterer locations for the data with an SNR of 10 dB. However, the FWHM values at all scatterer locations obtained from the data with an SNR of 5 dB are similar to those obtained from the data with an SNR of 10 dB. The significance of this observation is that it shows the SAFT performance is not affected by the SNR of the obtained data.

Similar results as those shown in figure 4.8 (b) at 10 dB SNR were observed in figure 4.13 (b) at 5 dB SNR. The FD-SAFT provided lower FWHM values than those obtained from the TD-SAFT and ATD-SAFT at almost all scatter locations. The TD-SAFT resulted in slightly lower FWHM values in comparison to the ATD-SAFT.

Figure 4.13 (c) shows the r_{FWHM} values, which increase as the distance of the scatterers from the virtual source increases, except for at 585 μm.

The side lobe values of the lateral profiles at the location of scatterers for the simulated data with an SNR of 5 dB are shown in figure 4.13 (d). The ATD-SAFT provided the lowest side lobe levels except for at 585 μm where f_{SL} of FD-SAFT was slightly lower than the f_{SL} value of ATD-SAFT. For the scatterers placed before the focus, FD-SAFT and TD-SAFT provided similar f_{SL} values. However, in the case of scatterers placed after the focus, the FD-SAFT provided lower f_{SL} values in comparison to those obtained from the TD-SAFT.

Similar conclusions are made on the performance of SAFT regardless of the SNR of the data; FD-SAFT and TD-SAFT provide similar FWHM values, which are better than those obtained from the ATD-SAFT, while the ATD-SAFT provides the lower side lobe levels than the FD-SAFT and TD-SAFT at almost all depths.

5.3 Experiments

Experiments were performed using the acoustic microscope introduced in section 3.1. SAFT is particularly suitable for acoustic microscopy because its transducer has a tight focus, which would be a good approximation to a virtual source in comparison to the focal region of a moderately focused transducer. In the case of a tight focus, the acoustic beam spreads wider beyond the focus.

It is important to analyze SAFT performance on experimental data as there are major differences between simulations and experiments. One of the main differences, that could effect the SAFT performance, is that the medium is inhomogeneous and dispersive. Moreover, scatterers do not scatter the acoustic wave isotropically. The micro beads used in the experiments are not equivalent to point scatterers as point scatterers have no physical size and scatter the incident wave isotropically. In addition, unlike the simulated data, the experimental data is subject to artifacts as described in section 3.1.2. In order to analyze the performance of an imaging system using the PSF, a small scatterer should be used, so that the scattering is as close to isotropic scattering as possible.

In the single bead experiments, a micro-bead of the diameter of approximately 2 μm, which was the smallest scatterer in the phantom, was used. Based on the images provided in section 4.2.1, it was observed that when the beads were placed after the focus of the transducer, the ATD-SAFT performed similar to the FD-SAFT, but the FD-SAFT performed better than the TD-SAFT and ATD-SAFT as the distance between the transducer and the scatterer was increased. When the beads were placed before the focus of the transducer, the FD-SAFT and TD-SAFT provided similar images and the ATD-SAFT provided the best image. It was observed that the ATD-SAFT image obtained from the bead placed 50 μm before the focus was slightly better than the one obtained when the bead was placed 50 μm after the focus. In all cases, the SAFT reconstructed images provided lower side lobe levels and better lateral resolution than the conventional

B-mode image.

Based on the images in section 4.2.2, SAFT is able to distinguish two scatterers that were close to each other, which could not be identified as individual scatterers in the conventional B-mode image even when the beads were placed at the focal region of the transducer. The best image improvement was obtained by the FD-SAFT and ATD-SAFT as the transducer distance from the scatterers was increased.

Experiments were also performed using a spheroid as the target in order to analyze the performance of SAFT in imaging scatterers that are closely placed and cannot be resolved with an acoustic microscope. However, since the internal structure of the spheroid is unknown and the obtained image has a lot of speckles, it was not possible to draw a conclusion on SAFT performance in imaging spheroids. As a result, the spheroid images were not used in analyzing the performance of SAFT as intended.

Chapter 6

Conclusions and Future Work

6.1 Conclusions

The synthetic aperture imaging technique improved the lateral resolution of both simulated and experimental images in comparison to the conventional B-mode imaging. Based on the simulations, it was concluded that the FD-SAFT and TD-SAFT provided similar FWHM values, which were better than those obtained with the ATD-SAFT, while the ATD-SAFT provided the lowest side lobe levels.

It was also concluded that, the SAFT algorithms provided lower FWHM values for the scatterers placed before the focus than those placed after the focus. However, the side lobe levels of the images of scatterers after the focus were lower than those of the before focus scatterers.

The experimental results agreed with the simulated outcomes as the SAFT reconstructed images provided improved lateral resolutions at different depths and lower side lobes levels in comparison to the conventional B-mode images. Two micro-beads that could not be distinguished from each other in a conventional B-mode image when placed far from the focus of the transducer were shown as individual structures in the SAFT reconstructed images.

Wiener filtering was effective in reducing the additive white Gaussian noise in all acoustic microscopy images.

In general, the SAFT algorithms outperformed the B-mode imaging technique in acoustic microscopy, especially when the scatterers were placed far from the focus. The FD-SAFT provided a good compromise between lateral resolution improvement and lowering the side lobe levels. However, when the ROI includes many scatterers, the ATD-SAFT provided a better image as opposed to the other SAFT algorithms.

The virtual source is limited to where the beams are relatively spherical in nature. It limits the reconstruction as scatterers at the focus cannot be reconstructed. Also, near the focus the beam is more planar than spherical. Therefore, the virtual source assumption is weak.

The relatively tight focusing of the acoustic microscope makes it more suitable for synthetic aperture imaging with a virtual source as the beam spreads over a larger aperture angle. Therefore, the focal spot of an acoustic microscope is closer to a point source in comparison to the focal spot of moderately focused ultrasound imaging systems.

6.2 Future Work

This thesis provides the first study of the application of SAFT algorithms for very high frequency (375 MHz) acoustic microscopy. It shows that SAFT is an improved image reconstruction technique when imaging objects are far from the focus of the microscope. The performance of SA image reconstruction algorithms is expected to improve by incorporating the diffraction effects of the transducer in the algorithms. The FD-SAFT is suitable for achieving this goal.

Acoustic microscopy is capable of performing 2D scanning. The SAFT algorithms can be easily modified to reconstruct 3D images of the ROI. The 3D data required for a 3D image reconstruction, can be obtained by stacking the 2D RF data in acoustic

microscopy.

Moreover, the implemented SAFT algorithms could be applied to optoacoustic imaging and optical coherent tomography.

Appendix A

Wiener Filtering

The system shown in figure 2.3 is required to be time-invariant, and consequently the desired estimate can be expressed as

$$\hat{S}(t) = \int_{-\infty}^{+\infty} h(t - \xi)Y(\xi)d\xi = \int_{0}^{+\infty} Y(t - \xi)h(\xi)d\xi \qquad (A.1)$$

For the random processes $S(t)$ and $Y(t)$, the autocorrelation, cross-correlation functions, and their Fourier transforms are denoted as the following, where $\mathcal{F}$ denotes the Fourier transform. where

Table A.1: Correlations and cross-correlations' notations

Function	Notation
autocorrelation of $S(t)$	$R_{ss}(t)$
autocorrelation of $Y(t)$	$R_{yy}(t)$
cross-correlation of $S(t)$ & $Y(t)$	$R_{sy}(t)$ & $R_{ys}(t)$
power spectral density of $S(t)$	$S_{ss}(f)$
power spectral density of $Y(t)$	$S_{yy}(f)$

$$R_{ss}(t) \overset{\mathcal{F}}{\Longleftrightarrow} S_{ss}(f)$$

$$R_{yy}(t) \overset{\mathcal{F}}{\Longleftrightarrow} S_{yy}(f)$$

$$R_{sy}(t) \overset{\mathcal{F}}{\Longleftrightarrow} S_{sy}(f)$$

$$R_{ys}(t) \overset{\mathcal{F}}{\Longleftrightarrow} S_{ys}(f)$$

Assume the power spectral density $S_{yy}(f)$ is a rational function and can be expressed as

$$S_{yy}(f) = S_{yy}^{+}(f).S_{yy}^{-}(f)$$

where $S_{yy}^{+}(f)$ and $S_{yy}^{-}(f)$ are called the spectral factorizations of $S_{yy}(f)$. $S_{yy}^{+}(f)$ have its poles and zeros in the left half-plane of the S-plane, whereas $S_{yy}^{-}(f)$ has all its poles and zeros in the right half-plane. The linear mean-square estimation requires that $h(t)$ be chosen so that the mean-square error is minimum. The transfer function of $h(t)$ can be expressed as

$$H(F) = \frac{B^{+}(f)}{S_{yy}^{+}(f)}$$

where, $B^{+}(f)$ is defined as

$$B^{+}(f) = \left[\frac{S_{sy}(f)}{S_{yy}(f)}\right]^{+}$$

Therefore, all the poles of $H(f)$ are in the left half-plane and consequently the filter response $h(t)$ is zero for negative time values ($t < 0$). Hence, the filter is realizable and causal. As a result, the optimum Wiener filter is

$$h(t) = \int_{-\infty}^{+\infty} \frac{B^{+}(f)}{S_{yy}^{+}(f)} e^{j2\pi ft} df \tag{A.2}$$

The corresponding minimum mean-square error is obtained by

$$e_m = E[(S - \hat{S})S] = \int_{-\infty}^{+\infty} \left[S_{ss}(f) - S_{sy}(-f) \frac{B^+(f)}{S_{yy}^+(f)} \right] df$$

Bibliography

[1] Michael C Kolios and Gregory J Czarnota. Potential use of ultrasound for the detection of cell changes in cancer treatment. *Future Oncology*, 5(10):1527–1532, 2009. PMID: 20001791.

[2] David J. Stephens and Victoria J. Allan. Light microscopy techniques for live cell imaging. *Science*, 300(5616):82–86, 2003.

[3] Gregory J Czarnota and Michael C Kolios. Ultrasound detection of cell death. *Imaging in Medicine*, 2(1):17–28, 2010.

[4] Michael C Kolios. Biomedical ultrasound imaging from 1 to 1000 MHz. *Canadian Acoustics / Acoustique Canadienne*, 37(3):35–42, 2009.

[5] R. A. Lemons and C. F. Quate. Acoustic microscope-scanning version. *Applied Physics Letters*, 24(4):163 –165, 1974.

[6] Eric Strohm. *Determining the Mechanical Properties of Apoptotic Cells Using Time Resolved Acoustic Microscopy*. MSc Thesis, Ryerson University, 2009.

[7] H-D Liang and M J K Blomley. The role of ultrasound in molecular imaging. *The British Journal of Radiology*, 76(2):S140–150, 2003.

[8] Jian-Yu Lu, Hehong Zou, and James F. Greenleaf. Biomedical ultrasound beam forming. *Ultrasound in Medicine and Biology*, 20(5):403 – 428, 1994.

[9] Richard S. C. Cobbald. *Foundations of Biomedical Ultrasound.* Oxford University Press, 2006.

[10] Nazanin Nayebi. *Synthetic Aperture Imaging: Applications in High-Frequency Ultrasound.* MSc Thesis, Ryerson University, 2008.

[11] Thomas. L. Szabo. *Diagnostic Ultrasound Imaging.* Elsevier Inc., 2004.

[12] Qifa Zhou, Dawei Wu, Changgeng Liu, Benpeng Zhu, F. Djuth, and K.K. Shung. Micro-machined high-frequency (80 MHz) PZT thick film linear arrays. *Ultrasonics, Ferroelectrics and Frequency Control, IEEE Transactions on*, 57(10):2213 –2220, 2010.

[13] Chang-Hong Hu, Xiao-Chen Xu, J.M. Cannata, J.T. Yen, and K.K. Shung. Development of a real-time, high-frequency ultrasound digital beamformer for high-frequency linear array transducers. *Ultrasonics, Ferroelectrics and Frequency Control, IEEE Transactions on*, 53(2):317 –323, 2006.

[14] C. Passmann and H. Ermert. In vivo imaging of the skin in the 100 MHz region using the synthetic aperture concept. In *IEEE Proceedings on Ultrasonics Symposium*, volume 2, pages 1287 –1290, 1995.

[15] M. Soumekh. *Synthetic Aperture Radar Signal Processing with MATLAB Algorithms.* John Wiley and Sons, 1999.

[16] V. Schmitz, S. Chakhlov, and W. Mller. Experiences with synthetic aperture focusing technique in the field. *Ultrasonics*, 38(1-8):731 – 738, 2000.

[17] Margaret Cheney. A mathematical tutorial on synthetic aperture radar. *SIAM Rev.*, 43:301–312, 2001.

[18] Jorgen Arendt Jensen, Svetoslav Ivanov Nikolov, Kim Lokke Gammelmark, and Morten Hogholm Pedersen. Synthetic aperture ultrasound imaging. *Ultrasonics*, 44(Supplement 1):e5 – e15, 2006.

[19] J. Opretzka, M. Vogt, and H. Ermert. A high-frequency ultrasound imaging system combining limited-angle spatial compounding and model-based synthetic aperture focusing. *Ultrasonics, Ferroelectrics and Frequency Control, IEEE Transactions on*, 58(7):1355 –1365, 2011.

[20] K. Nagai. Fourier domain reconstruction of synthetic focus acoustic imaging system. *Proceedings of the IEEE*, 72(6):748 – 749, 1984.

[21] H. Ermert and R. Karg. Multifrequency acoustical holography. *Sonics and Ultrasonics, IEEE Transactions on*, 26(4):279 – 285, 1979.

[22] T. Stepinski. An implementation of synthetic aperture focusing technique in fequency domain. *IEEE Transactions on Ultrasonics, Ferroelectrics, and Frequency Control*, 54(7):1399–1408, 2007. cited By (since 1996) 9.

[23] C. Passmann and H. Ermert. A 100-MHz ultrasound imaging system for dermatologic and ophthalmologic diagnostics. *Ultrasonics, Ferroelectrics and Frequency Control, IEEE Transactions on*, 43(4):545 –552, 1996.

[24] C.H. Frazier and Jr. O'Brien, W.D. Synthetic aperture techniques with a virtual source element. *IEEE Transactions on Ultrasonics, Ferroelectrics and Frequency Control*, 45(1):196 –207, 1998.

[25] M. Karaman, Pai-Chi Li, and M. O'Donnell. Synthetic aperture imaging for small scale systems. *Ultrasonics, Ferroelectrics and Frequency Control, IEEE Transactions on*, 42(3):429 –442, 1995.

[26] G.R. Lockwood, J.R. Talman, and S.S. Brunke. Real-time 3-d ultrasound imaging using sparse synthetic aperture beamforming. *Ultrasonics, Ferroelectrics and Frequency Control, IEEE Transactions on*, 45(4):980 –988, 1998.

[27] S. Nikolov, K. Gammelmark, and J.A. Jensen. Recursive ultrasound imaging. In *IEEE Ultrasonics Symposium*, volume 2, pages 1621 –1625 vol.2, 1999.

[28] J.A. Jensen and N.B. Svendsen. Calculation of pressure fields from arbitrarily shaped, apodized, and excited ultrasound transducers. *IEEE Transactions on Ultrasonics, Ferroelectrics and Frequency Control*, 39(2):262 –267, 1992.

[29] G. E. Tupholme. Generation of acoustic pulses by baffled plane pistons. *Mathematika*, 16(2):209 – 224, 1969.

[30] P. R. Stepanishen. The time dependent force and radiation impedance on a piston in a rigid infinite planar baffle. *The Journal of the Acoustical Society of America*, 49(3B):841–849, 1971.

[31] Gerald R. Harris. Review of transient field theory for a baffled planar piston. 70(1):10–20, 1981.

[32] J.A. Jensen, D. Gandhi, and Jr. O'Brien, W.D. Ultrasound fields in an attenuating medium. In *IEEE Ultrasonics Symposium*, volume 2, pages 943 –946, 1993.

[33] M. O'Donnell and Jr. Riley, H.F. Clinical evaluation of the B-scan. *IEEE Transactions on Sonics and Ultrasonics,*, 32(3):450 – 457, 1985.

[34] John R. Buck Alan V. Oppenheim, Ronald W. Schafer. *Discrete-Time Signal Processing*. Prentice Hall, 1999.

[35] Mourad Barkat. *Signal Detection and Estimation*. Artech House Publishers, 2005.

[36] F. Lingvall, T. Olofsson, and T. Stepinski. Synthetic aperture imaging using sources with finite aperture: Deconvolution of the spatial impulse response. *Journal of the Acoustical Society of America*, 114(1):225–234, 2003.

[37] T. Taxt and J. Strand. Two-dimensional noise-robust blind deconvolution of ultrasound images. *IEEE Transactions on Ultrasonics, Ferroelectrics and Frequency Control*, 48(4):861 –866, 2001.

[38] O.V. Michailovich and D. Adam. A novel approach to the 2-d blind deconvolution problem in medical ultrasound. *IEEE Transactions on Medical Imaging,*, 24(1):86 –104, 2005.

[39] J. Ng, R. Prager, N. Kingsbury, G. Treece, and A. Gee. Wavelet restoration of medical pulse-echo ultrasound images in an em framework. *IEEE Transactions on Ultrasonics, Ferroelectrics and Frequency Control*, 54(3):550 –568, 2007.

[40] Meng-Lin Li, Wei-Jung Guan, and Pai-Chi Li. Improved synthetic aperture focusing technique with applications in high-frequency ultrasound imaging. *IEEE Transactions on Ultrasonics, Ferroelectrics and Frequency Control*, 51(1):63 –70, 2004.

[41] Moo-Ho Bae and Mok-Kun Jeong. A study of synthetic-aperture imaging with virtual source elements in b-mode ultrasound imaging systems. *IEEE Transactions on Ultrasonics, Ferroelectrics and Frequency Control*, 47(6):1510 – 1519, 2000.

[42] T. Stepinski. An implementation of synthetic aperture focusing technique in frequency domain. *IEEE Transactions on Ultrasonics, Ferroelectrics and Frequency Control*, 54(7):1399 –1408, 2007.

[43] T. Stepinski and F. Lingvall. Optimized algorithm for synthetic aperture imaging. In *IEEE Ultrasonics Symposium*, volume 1, pages 701 – 704, 2004.

[44] `http://www.kibero.com/html/technology.htm`.

[45] W. Bost, F. Stracke, E.C. Weiss, S. Narasimhan, M.C. Kolios, and R. Lemor. High frequency optoacoustic microscopy. In *Annual International Conference of the IEEE Engineering in Medicine and Biology Society*, pages 5883 –5886. IEEE EMBS, 2009.

[46] Andrew Briggs. *An Introduction to Scanning Acoustic Microscopy.* Oxford University Press, 1985.

[47] J.A. Jensen. *User's guide for the Field II program.* Technical University of Denmark, 2001.

[48] J.A. Jensen. Simulation of advanced ultrasound systems using field II. In *IEEE International Symposium on Biomedical Imaging: Nano to Macro.*, pages 636 – 639, 2004.

[49] S. Inglis, K.V. Ramnarine, J.N Plevris, and W.N McDicken. An anthropomorphic tissue-mimicking phantom of the oesophagus for endoscopic ultrasound. *Ultrasound in Medicine and Biology*, 32(2):249 – 259, 2006.